Uncl

SECURITY

AD-A240 004

ITATION PAGE

Form Approved
OMB No. 0704-0188

2

1a. REPOR
Unclassified

1b RESTRICTIVE MARKINGS

2a. SECURITY CLASSIFICATION AUT

2b. DECLASSIFICATION / DOWNGRAD SCHEDULE

DTIC
ELECTE
SEP 0 5 1991
S D
D

3. DISTRIBUTION / AVAILABILITY OF REPORT
Approved for public release;
distribution is unlimited

4 PERFORMING ORGANIZATION R NUMBER(S)
None

5. MONITORING ORGANIZATION REPORT NUMBER(S)
AFOSR-TR- 91 071~~1~~5

6a NAME OF PERFORMING ORGANIZATION
Pennsylvania State University

6b. OFFICE SYMBOL *(If applicable)*

7a. NAME OF MONITORING ORGANIZATION
AFOSR/NA

6c. ADDRESS *(City, State, and ZIP Code)*
Mechanical Engineering Department
University Park, PA 16802

7b. ADDRESS *(City, State, and ZIP Code)*
Building 410, Bolling AFB DC
20332-6448

8a NAME OF FUNDING / SPONSORING ORGANIZATION
AFOSR/NA

8b. OFFICE SYMBOL *(If applicable)*
NA

9. PROCUREMENT INSTRUMENT IDENTIFICATION NUMBER
AFOSR-89-0312

8c. ADDRESS *(City, State, and ZIP Code)*
Building 410, Bolling AFB DC
20332-6448

10. SOURCE OF FUNDING NUMBERS

PROGRAM ELEMENT NO.	PROJECT NO.	TASK NO.	WORK UNIT ACCESSION NO.
61102F	2308	A1	

11. TITLE *(Include Security Classification)*
(U)
Coupling Between Radiation and Gas Dynamics

12. PERSONAL AUTHOR(S)
Charles L. Merkle and Michael M. Micci

13a. TYPE OF REPORT
Final

13b. TIME COVERED
FROM 01 Feb90 TO 01 Feb91

14. DATE OF REPORT *(Year, Month, Day)*
1991, May 31

15. PAGE COUNT

16. SUPPLEMENTARY NOTATION

17. COSATI CODES

FIELD	GROUP	SUB-GROUP

18. SUBJECT TERMS *(Continue on reverse if necessary and identify by block number)*
Electrothermal Propulsion
Microwave-heated Plasmas
Microwave-Gasdynamic Interaction
Microwave-heated Thrusters
Beamed Energy
Advanced Propulsion

19. ABSTRACT *(Continue on reverse if necessary and identify by block number)*

Detailed experimental and analytical studies of microwave thermal propulsion are presented and discussed. Results are obtained for four specific geometrical configurations: bluff-body stabilized resonant cavity plasmas, swirl-stabilized resonant cavity plasmas, free-floating plasmas in resonant cavities, and propagating, bluff-body stabilized plasmas in waveguides. Swirl stabilization proved to be less effective than bluff-body stabilization and was not modeled analytically. The experimental studies included both helium and nitrogen plasmas, while the analytical results are for helium only. In the free-floating plasmas, non-axisymmetric effects in the experimental setup led to arcing to the wall, limiting maximum power levels to about 500 W, although the analysis suggests substantially higher upper power levels for this configuration. The bluff-body stabilized, resonant cavity plasmas, however, allowed power absorptions up to the maximum source power of 2.5 kW and 5 atm pressure for helium, although experiments in nitrogen were limited to lower powers.

(Cont'd on reverse)

20. DISTRIBUTION / AVAILABILITY OF ABSTRACT
☒ UNCLASSIFIED/UNLIMITED ☒ SAME AS RPT. ☑ DTIC USERS

21. ABSTRACT SECURITY CLASSIFICATION
Unclassified

22a. NAME OF RESPONSIBLE INDIVIDUAL
Dr Mitat Birkan

22b. TELEPHONE *(Include Area Code)*
(202) 767-4937

22c. OFFICE SYMBOL
AFOSR/NA

DD Form 1473, JUN 86

Previous editions are obsolete.

SECURITY CLASSIFICATION OF THIS PAGE
Unclassified

91 9 5 025

19. ABSTRACT (Continued from front)

The analytical predictions agree well with the experiments in terms of plasma size, location, and response to parameters such as input power, mass flow rate, electromagnetic wave form, and pressure. In addition, the predicted coupling efficiencies and peak temperatures are in good agreement with measurements. Coupling efficiencies of near 100% can be obtained for the resonant cavity configurations, with somewhat lower efficiencies for the propagating plasmas. Major research issues that remain include identifying means for increasing the average temperature while maintaining appropriate wall heat fluxes, and potential means for size scale-up in microwave thrusters. The analysis indicates higher mean temperatures can be obtained by increasing the size of the bluff-body stabilizer, and by increasing the power of the microwave source.

FINAL REPORT

on

COUPLING BETWEEN RADIATION
AND GAS DYNAMICS

Submitted to:

Dr. Mitat Birkan
Air Force Office of Scientific Research
Directorate of Aerospace Sciences
Bolling Air Force Base, D.C. 20332

by

Dr. Charles L. Merkle
Mechanical Engineering Department
The Pennsylvania State University
University Park, PA 16802
(814) 863-1501

and

Dr. Michael M. Micci
Aerospace Engineering Department
The Pennsylvania State University
University Park, PA 16802
(814) 863-0043

May 1991

TABLE OF CONTENTS

Page

COUPLING BETWEEN GAS DYNAMICS AND MICROWAVE ENERGY ABSORPTION
(Michael M. Micci)

COUPLING BETWEEN GAS DYNAMICS AND MICROWAVE ENERGY ABSORPTION
(Charles L. Merkle)

Final Report

on

COUPLING BETWEEN GAS DYNAMICS AND MICROWAVE ENERGY ABSORPTION

Submitted to:

Dr. Mitat Birkan
Air Force Office of Scientific Research
Directorate of Aerospace Sciences
Bolling Air Force Base, D.C. 20332

by

Dr. Michael M. Micci
Aerospace Engineering Department
and
Propulsion Engineering Research Center
The Pennsylvania State University
University Park, PA 16802
(814) 863-0043

April 1991

Work Statement

1. Determine experimentally the conditions under which free-floating nitrogen and helium plasmas can be initiated and sustained in the TE_{01} mode microwave resonant cavity. Measure maximum obtainable gas pressure and temperature and coupling efficiency as a function of input power and gas flow rate. Spectroscopic measurements of temperature and electron density will not assume complete LTE. Compare results to those obtained for the TM_{01} mode.

2. Examine the effect of various plasma stabilization schemes in a microwave resonant cavity on maximum obtainable gas pressure and temperature and coupling efficiency. Quantify the losses caused by the introduction of the plasma stabilization schemes.

3. Modify the numerical model of the microwave-heated propagating plasma to incorporate the effects of energy transfer to the cold upstream gas by resonant radiation. Compare numerical results to experimentally measured values.

4. Examine the effects of various techniques to spatially stabilize experimentally generated propagating plasmas. Measure plasma and gas temperature and coupling efficiencies as a function of input power for the stabilized plasmas.

1.0 Status of Research Effort

Experiments in the previous grant year with free-floating resonant cavity plasmas indicated that the maximum input power was restricted to below approximately 500 W, above which the plasma was observed to move towards the wall of the quartz vessel, resulting in rapid heating of the quartz. It is believed that this instability is due to the asymmetric introduction of microwave power to the cavity, which results in a perturbation of the electric field pattern from the axisymmetric pattern which would otherwise be expected. In order to overcome this instability and allow the maximum available power to be input to the resonant cavity (2.5 kW) two fluid dynamic stabilization schemes, bluff body and swirling flow, were examined this year. Both these schemes have been used extensively in combustion systems and to some extent in previous electrothermal propulsion systems involving plasmas. The bluff body creates a recirculation region with a decreased pressure and increased residence time while enhancing mixing in the region behind the bluff body while swirling flows also create a region of decreased pressure and a recirculating flow without the fluid dynamic drag associated with the bluff body and the heat transfer to the bluff body.

The plasma containment vessel used in these experiments was a quartz hemisphere of 75 mm diameter with a boron nitride flange at the downstream end containing a choked orifice. The bluff body and flow swirler were also fabricated from boron nitride. Both helium and nitrogen plasmas were investigated and the resonant cavity was operated in the TM_{011} mode (compared to the TM_{012} mode used for the free-floating plasmas), which gave a region of maximum electric field strength in the region between the flow stabilizer and the choked orifice. Maximum gas pressure available with the experimental system was 500 kPa (5 atmospheres).

It was found that bluff-body stabilization proved more effective in allowing operation at higher input microwave power levels and gas pressures than the flow swirler, although the poor performance of the flow swirler may be due to its installation upstream of the hemispherical quartz vessel and the resulting expansion of the flow as it enters the hemisphere. Thus the majority of the experiments were carried out using the bluff body. It was also found that with the bluff body nitrogen plasmas could only be sustained at powers less than 700 W and gas pressures less than 170 kPa before becoming unstable and moving to the wall of the quartz vessel, whereas helium plasmas could be sustained up to the maximum available microwave power of 2.5 kW and gas pressure of 500 kPa. The majority of the measurements were thus made with helium plasmas.

Figure 1 shows the ability of the bluff body to raise the maximum microwave power and gas pressure while keeping a helium plasma centered in the resonant cavity. The points plotted for the TM_{012} mode are for the free-floating plasma where higher input powers resulted in the plasma moving to the wall of the resonant cavity. The points plotted for the TM_{011} mode are for the bluff-body stabilized plasma. It can been that for low power levels the results for the two modes coincide while the bluff body allows operation at much higher power levels and gas pressures. The maximum gas pressures of 500 kPa at 1000 and 1500 W do not indicate that the plasma cannot be sustained at higher pressures but is only the limitation of the experimental system. At these points no increase of reflected power from the cavity was observed, an increase which serves as an indication of approaching the extinction limit.

The coupling efficiency is a measure of the percentage of the input microwave power which is absorbed by the cavity and is the ratio of the input power minus the reflected power divided by the input power. Figure 2 plots the coupling efficiency as a function of gas pressure for bluff-body stabilized helium plasmas for input powers from 1.25 to 2 kW. It can be seen that the coupling efficiency increases with pressure, with higher input powers requiring higher pressures to obtain their maximum coupling efficiency. In those cases where the experimental system permitted a sufficiently high pressure to reach the maximum, coupling efficiencies close to 100% where obtained. Even with the low powers and pressures which allowed a stable nitrogen plasma, coupling efficiencies approaching 100% were obtained. These results are much higher than the 80% coupling efficiencies obtained with the free-floating helium and nitrogen plasmas operating in the TM_{012} mode because the bluff-body stabilization permitted more optimal tuning of the cavity without the plasma moving to the wall of the quartz vessel, thus indicating another advantage of the fluid dynamic stabilization provided by the bluff body.

The overall efficiency of the microwave electrothermal thruster is the ratio of the power of the gas exiting through the choked orifice to the input microwave power. The power of the gas exiting through the choked orifice was determined by the mean stagnation temperature of the gas and the mass flow rate. The mean stagnation temperature of the gas was determined by measuring the stagnation pressure and mass flow rate through the quartz vessel and knowing the area of the choked orifice. Figure 3 plots the overall efficiency of bluff-body stabilized helium plasmas as a function of specific power (microwave power absorbed by the plasma divided by the mass flow) for input powers from 500 W to 2 kW. The processes which cause an overall efficiency of less than 100% are conductive losses to the bluff body, orifice plate and quartz walls, reflected power from the cavity, ohmic losses in the cavity walls and radiative losses from the plasma, which will be absorbed by either the quartz vessel or the surrounding cavity. For a given input power the specific power was increased by decreasing the chamber pressure and therefore the mass flow rate through the choked orifice. It can be seen that the overall efficiency decreases with decreasing pressure (and therefore mass flow rate) and increasing power. This may be explained by considering the physical behavior of the plasma as these parameters are varied. Increasing the pressure reduced the plasma diameter. In the region where the plasma is stably located downstream of the bluff body, this reduction in plasma diameter has the effect of reducing the heat load to the quartz vessel and thus increasing the overall efficiency. Increasing the input power has the effect of increasing the plasma diameter (as well as the plasma length), increasing the conductive losses to the bluff body, orifice plate and quartz vessel, therefore reducing the overall efficiency.

Assuming an isentropic expansion to vacuum conditions, the specific impulse of the microwave electrothermal thruster was calculated. It was found that the specific impulse increased linearly with specific power, reaching a maximum value of 543 s for the helium plasma. The use of hydrogen propellant under the same operating conditions would produce a specific impulse of 1086 s due to the decrease of molecular weight (assuming complete dissociation, which would be expected at the plasma temperatures achieved) by a factor of four.

Spectroscopic measurements were made of the helium plasma temperature as a function of the operating conditions. The spectroscopic system consisted of a Czerny-Turner half meter spectrometer and an electronically tunable Fabry-Perot etalon. Electron temperatures were measured using the absolute continuum method. Calibration of the system was accomplished by using a calibrated tungsten strip lamp and the Saha equation was used to obtain the electron number density as a function of temperature (the electron number density being a required input parameter to determine the electron temperature via this method). Measurements of the Doppler broadened line width were used to determine the heavy particle (ions and neutrals) temperature. Radial profiles of electron temperature were measured using an Abel inversion. It was found that the electron temperature at the center of the plasma was insensitive to variations in input power and gas pressure, varying from 11,880 to 12,170 K as the input power was varied from 500 to 1000 W and the gas pressure from 120 to 300 kPa (absolute). This insensitivity corresponds to results published in previous literature for microwave-heated argon and hydrogen plasmas. Radial profiles of the electron temperature from the center to the edge of the plasma were found to be flat, decreasing approximately 10% from the center to the edge. Measurements of the heavy particle temperature were more sensitive to the light intensity measurements and therefore produced greater scatter in the results, however the data scatter bounded the measured electron temperatures with the conclusion that the electron and heavy particle temperatures are approximately equal.

Because the resonant cavity and waveguide experiments could not be conducted simultaneously since they both required the same microwave power source, the final experiments with the propagating microwave waveguide plasmas could not be completed by the end of the grant period. However these experiments are continuing under support by the NASA Propulsion Engineering Research Center at Penn State. Previous experiements with bluff-body stabilized helium and nitrogen waveguide plasmas used a rectangular waveguide which produced a plasma which extended from one wall of the waveguide to the other due to the electric field pattern propagating through the waveguide. This plasma geometry is not desirable from a propulsion standpoint because of the contact between the plasma and the walls of the waveguide and the associated erosion and heat transfer losses. A cylindrical waveguide was designed and manufactured which propagates an electric field where the field maxima are in the interior of the waveguide, producing a plasma which is centrally located, not making contact with the walls of the cavity. A bluff body is once again used to provide fluid dynamic stabilization of the plasma with the flow exiting through a choked orifice. Experiments are currently underway with helium plasmas to measure stability boundaries, coupling efficiencies, overall efficiencies and electron and heavy particle temperatures as a function of input microwave power and gas pressure.

Cumulative Chronological List of Written Publications in Technical Journals

1. Knecht, J. P. and Micci, M. M., "Analysis of a Microwave-Heated Planar Propagating Hydrogen Plasma," AIAA Journal, Vol. 26, No. 2, Feb. 1988, pp. 188-194.

2. Balaam, P. and Micci, M. M., "Microwave Electrothermal Propulsion Utilizing Free-Floating Resonant Cavity Plasmas," Scheduled for publication in Journal of Propulsion and Power.

3. Mueller, J. and Micci, M. M., "Microwave Waveguide Helium Plasmas for Electrothermal Propulsion," Submitted to Journal of Propulsion and Power, Jan. 1991.

Professional Personnel Associated with Research Effort

Professional Staff

Michael M. Micci, Associate Professor, Aerospace Engineering

Graduate Students

James P. Knecht, Graduate Assistant, January 1985-May 1986. M. S. Thesis title, "Numerical Analysis of a Microwave-Heated Planar Propagating Hydrogen Plasma." Present Position: MIT Lincoln Labs, Lexington, MA.

William Maul, Graduate Assistant, June 1985-December 1987. M. S. Thesis title, "The Characteristics of a Stationary Free-Floating Nitrogen Discharge Generated in a Microwave Resonant Cavity." Present Position: SVERDRUP, Cleveland, OH.

Philip Balaam, Graduate Assistant, August 1987-December 1990. Ph.D. Thesis title, "The Experimental Development of a Microwave Resonant Cavity Electrothermal Thruster." Present Position: Matra, Toulouse, France.

Juergen Mueller, Graduate Assistant, August 1987-present. Anticipated Ph.D. Thesis title, "Analytical and Experimental Study of Propagating Microwave-Heated Plasmas."

Interactions

(1) Spoken papers

Coupling Between Gas Dynamics and Microwave Energy Absorption. Presented at the AFOSR/AFRPL Rocket Propulsion Research Meeting, March 21, 1985, Lancaster, CA.

Prospects for Microwave Heated Propulsion. Presented at Aerojet Tech Systems, Sacramento, CA, Oct. 8, 1985.

Prospects for Microwave Heated Propulsion. Presented to Project Forecast II, November 19, 1985, Arlington, VA.

Coupling Between Gas Dynamics and Microwave Energy Absorption. Presented at the AFOSR/AFRPL Rocket Propulsion Research Meeting, September 11, 1986, Lancaster, CA.

Microwave Electrothermal Propulsion. Presented at the Air Force Office of Scientific Research, Bolling AFB, DC, September 18, 1986.

Analysis of Propagating Microwave Heated Plasmas in Hydrogen, Helium and Nitrogen. Presented at the 19th AIAA/DGLR/JSASS International Electric Propulsion Conference, May 12, 1987, Colorado Springs, CO.

Coupling Between Gas Dynamics and Microwave Energy Absorption. Presented at the AFOSR/ONR Combustion and Rocket Propulsion Contractors Meeting, June 26, 1987, State College, PA.

Microwave Electrothermal Propulsion. Presented at Purdue University, July 13, 1987, W. Lafayette, IN.

Microwave Electrothermal Propulsion. Presented at The Ohio State University, September 8, 1987, Columbus, OH.

Coupling Between Gas Dynamics and Microwave Energy Absorption. Presented at the AFOSR/ONR Contractors Meeting, June 13-17, 1988, Pasadena, CA.

Characteristics of Free-Floating Nitrogen and Helium Plasmas Generated in a Microwave Resonant Cavity (with P. Balaam and W. Maul). Presented at the DGLR/AIAA/JSASS 20th International Electric Propulsion Conference, Garmisch-Partenkirchen, W. Germany, October 3-6, 1988.

Numerical and Experimental Investigations of a Propagating Microwave-Heated Plasma (with J. Mueller). Presented at the DGLR/AIAA/JSASS 20th International Electric Propulsion Conference, Garmisch-Partenkirchen, W. Germany, October 3-6, 1988.

Microwave-Heated Plasmas for Use in Space Propulsion. Presented to the Department of Nuclear Engineering, The Pennsylvania State University, Nov. 8, 1988, University Park, PA.

Coupling Between Gas Dynamics and Microwave Energy Absorption. Presented at the AFOSR/ONR Contractors Meeting, June 19-23, 1989, Ann Arbor, MI.

Investigation of Free-Floating Nitrogen and Helium Plasmas Generated in a Microwave Resonant Cavity (with P. Balaam). Presented at the AIAA/ASME/SAE/ASEE 25th Joint Propulsion Conference, Monterey, CA, July 10-12, 1989.

Investigation of Propagation Mechanism and Stabilization of a Microwave Heated Plasma (with J. Mueller). Presented at the AIAA/ASME/SAE/ASEE 25th Joint Propulsion Conference, Monterey, CA, July 10-12, 1989.

Coupling Between Gas Dynamics and Microwave Energy Absorption. Presented at the AFOSR/ONR Contractors Meeting, June 1990, Atlanta, GA.

Microwave Electrothermal Thruster Using Waveguide Heated Plasmas (with J. Mueller). Presented at the AIAA/DGLR/JSASS 21st International Electric Propulsion Conference, Orlando, FL, July 18-20, 1990.

The Stabilization and Spectroscopic Study of Microwave Generated Resonant Cavity Plasmas (with P. Balaam). Presented at the AIAA/DGLR/JSASS 21st International Electric Propulsion Conference, Orlando, FL, July 18-20, 1990.

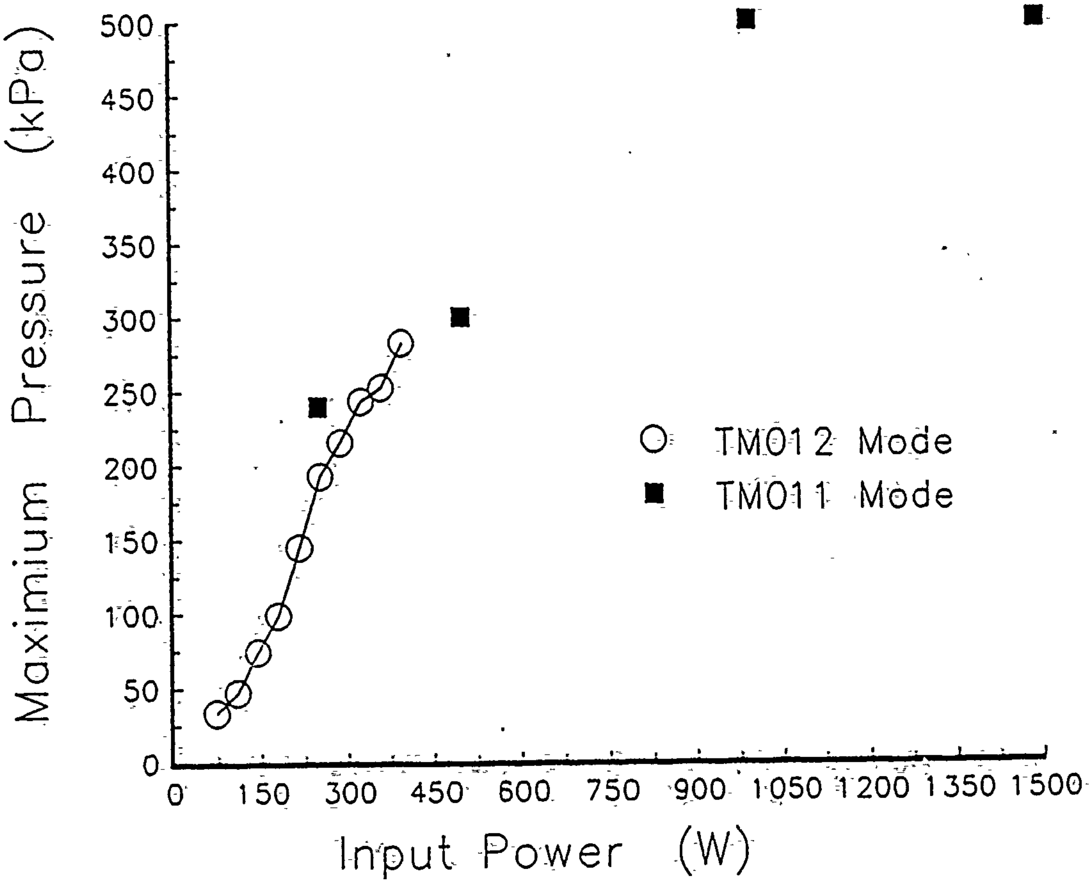

Fig. 1 Stability boundaries for helium plasmas for both the free-floating TM_{012} and the bluff-body stabilized TM_{011} modes showing the effectiveness of bluff-body stabilization.

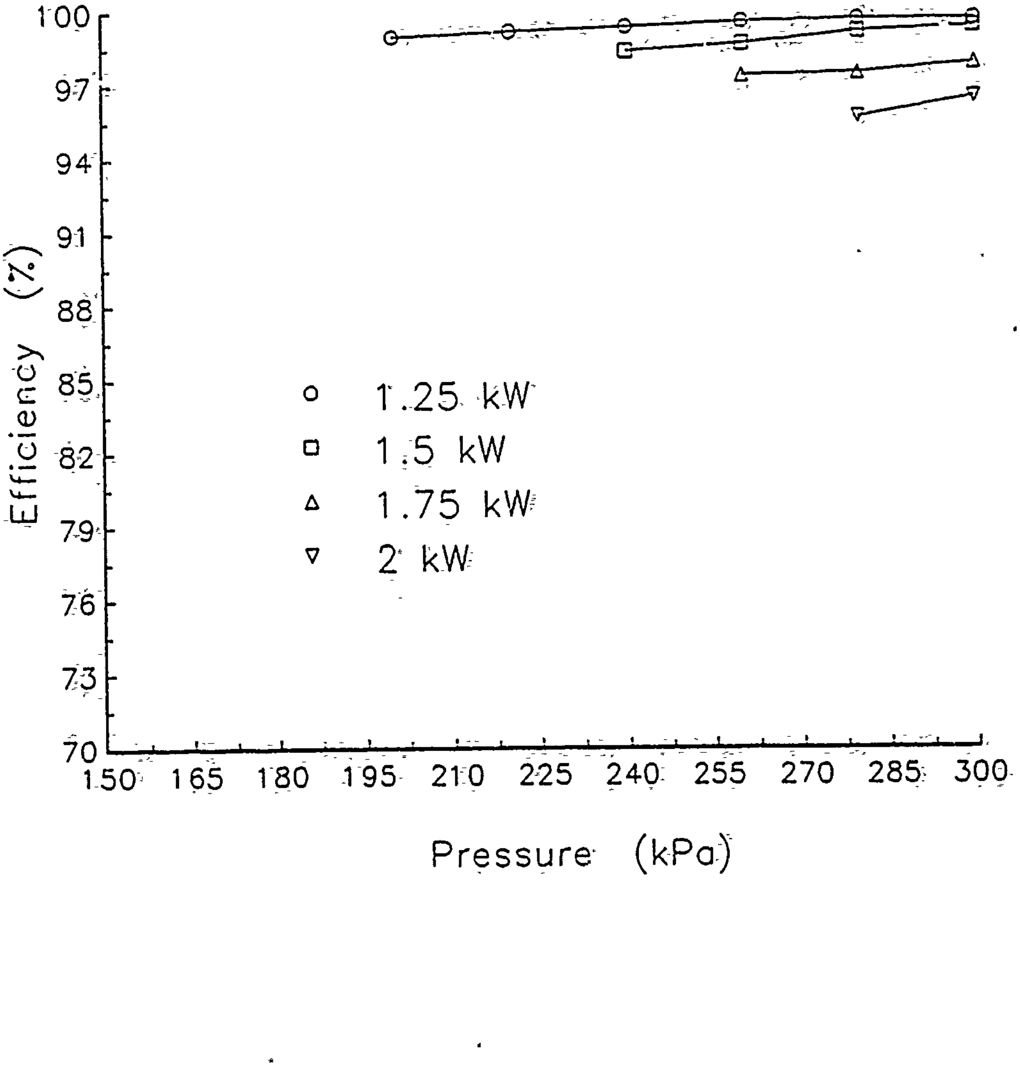

Fig. 2 Coupling efficiencies for bluff-body stabilized helium plasmas as a function of pressure for input powers from 1.25 to 2 kW. Higher powers require higher pressures for optimal coupling efficiency.

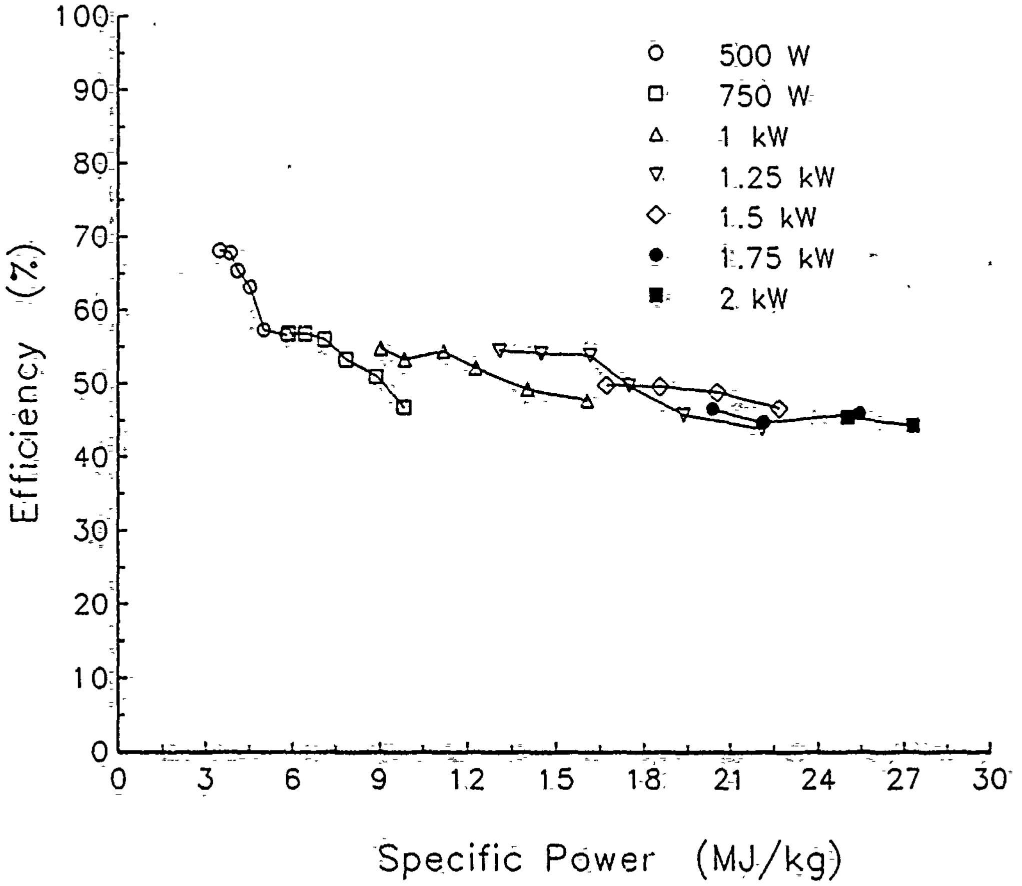

Fig. 3 Calculated overall efficiencies versus specific power for bluff-body stabilized helium plasmas showing a decrease in overall efficiency down to a minimum of 45% with an increase in specific power.

Final Report

on

COUPLING BETWEEN GAS DYNAMICS AND MICROWAVE ENERGY ABSORPTION

Submitted to:

Dr. Mitat Birkan
Air Force Office of Scientific Research
Directorate of Aerospace Sciences
Bolling Air Force Base, D.C. 20332

by

Dr. Charles L. Merkle
Mechanical Engineering Department
The Pennsylvania State University
University Park, PA 16802
(814) 863-1501

May 1991

2.0 DESCRIPTION OF THE COMPUTATIONAL MODEL

The computational model for microwave thermal propulsion is based upon the simultaneous numerical solution of the Maxwell and Navier-Stokes equations. These equations are strongly coupled to each other through the electrical conductivity of the gas which acts as a source term in the energy equation to absorb the microwaves, and also as a parameter in the Maxwell equations that determine the electromagnetic field distribution. Although previous analyses of radio frequency plasmas [1-3] have solved the Maxwell equations in the frequency domain, the present analysis solves the complete time-dependent equations in the physical domain. The harmonic analysis is suitable when the fundamental mode is of interest, but its convergence is seriously impaired for higher modes such as the TM012 and the TM011 modes that are of interest here. In particular, an explicit time-dependent approach similar to Yee's [4] is chosen. The RMS values of the fields required in the Navier-Stokes equations are determined by averaging the instantaneous E-M field over the wave period. To find this value, the E-M equations are solved over one (or several) wave period(s) at each time step of the Navier-Stokes equations. Because the explicit scheme used for the Maxwell equations is extremely rapid, this procedure causes less than a factor of two increase in the CPU time required as compared to the Navier-Stokes equations alone.

Parametric solutions have been obtained for three basic geometrical configurations for microwave absorption, the free-floating plasma in a resonant cavity, the bluff-body stabilized plasma in a resonant cavity, and the bluff-body stabilized plasma in a waveguide. These three geometrical configurations are identical to the three experimental configurations that have been tested, and comparisons with experiment are given for all three geometries. The same analysis is used for all three configurations. This model and the numerical solution technique is outlined in this section, followed by a summary of the results in the following section.

2.1 Geometric Configurations

The three geometric configurations considered are given in Figs. 1 and 2. Figure 1a shows the geometry for the free-floating resonant cavity plasma, while Fig. 1b represents the bluff-body stabilized resonant cavity plasma and Fig. 2 depicts the bluff-body stabilized, waveguide heated plasma. The free-floating resonant cavity plasma in Fig. 1a consists of a sphere-cylinder tube arrangement that passes through the microwave cavity. The tube diameter is 2.5 cm while the sphere diameter is 10 cm. In general, a TM012 mode is set up in the cavity, and is used to sustain a microwave plasma in the spherical section of the cavity. To understand the details of the fluid dynamic interactions in this geometry better, we have also computed solutions for a sphere-cylinder combination with a tube diameter of 7.5 cm, and a straight tube configuration in which the entire flowfield is cylindrical in nature (no broadened spherical region), with a diameter of 10 cm. Examples of these special geometries are given later. In all cases, the flow is from top to bottom, with gravitational forces acting in the downward direction.

The geometrical details of the flow tube and the microwave cavity for the bluff-body stabilized resonant cavity plasma are described in Fig. 1b. The gas again flows from top to bottom in a cylindrical tube with a diameter of 4 cm, with a wider bulb at the bottom. The bulb expands out to a diameter of 8 cm, and the gas exits from this bulb through a small, choked hole in the bottom. The bluff body is a small triangular-shaped (non-conducting) body with a base diameter of 2 cm. In the experiments, the bluff body can be moved axially up and down to find the most "effective" location for the plasma. The standing electromagnetic field pattern in this configuration is a TM011 mode. The plasma again forms at one of the peaks in the standing mode. A second alternate geometry is also used for broadened understanding in this geometrical configuration.

The waveguide configuration is a straight tube configuration (Fig. 2) with a bluff body similar to that described above centered in the straight part of the tube. It again has a diameter of 2 cm, although a larger 4.5 cm bluff body is also used for some of the calculations to determine the effect of the bluff body size on the plasma behavior. For this configuration, the microwaves are not set up in a standing wave pattern but, rather, are allowed to propagate through the plasma region. The absorption efficiencies observed for this configuration are somewhat lower than for the two standing wave cases. Two different downstream end conditions are, however, used for the microwaves in this geometry to again identify the important effects. The first end condition is a fully transmitting condition, while the second is a fully reflecting condition. The presence of a reflecting end condition gives rise to a weak standing wave pattern that in many ways behaves like a resonant cavity. Once again, flow in this configuration is from top to bottom.

2.2 Fluid Dynamic Model

The equations of motion that govern the flow of gaseous helium are the compressible Navier-Stokes equations. Because of the low Mach numbers encountered in the flow, we use the low Mach number formulation described by Choi and Merkle. The low Mach number version of the equations possesses well-conditioned eigenvalues at arbitrarily low Mach numbers and thus ensures robust convergence of the time-marching algorithm. For purposes of the numerical algorithm, the equations are written in the coupled vector form including the unsteady terms:

$$P\frac{\partial Q}{\partial t} + \frac{\partial E}{\partial x} + \frac{\partial F}{\partial y} = \frac{\partial E_v}{\partial x} + \frac{\partial F_v}{\partial y} + H_1 + H_2, \qquad (1)$$

where

$$P = \begin{pmatrix} 1 & 0 & 0 & 0 \\ u & \rho & 0 & 0 \\ v & 0 & \rho & 0 \\ T & 0 & 0 & \rho \end{pmatrix}, \qquad Q = \begin{pmatrix} p_1 y/\beta \\ uy \\ vy \\ Ty \end{pmatrix},$$

$$E = \begin{pmatrix} \rho uy \\ (\rho u^2 + \epsilon p_1)y \\ \rho uvy \\ \rho uTy \end{pmatrix}, \qquad F = \begin{pmatrix} \rho vy \\ \rho uvy \\ (\rho v^2 + \epsilon p_1)y \\ \rho vTy \end{pmatrix},$$

$$E_v = \begin{pmatrix} 0 \\ \frac{4}{3}\mu y\frac{\partial u}{\partial x} - \frac{2}{3}\mu y\frac{\partial v}{\partial y} \\ \mu y\frac{\partial v}{\partial x} + \mu y\frac{\partial u}{\partial y} \\ K_c y\frac{\partial T}{\partial x} \end{pmatrix}, \qquad F_v = \begin{pmatrix} 0 \\ \mu y\frac{\partial v}{\partial x} + \mu y\frac{\partial u}{\partial y} \\ -\frac{2}{3}\mu y\frac{\partial u}{\partial x} + \frac{4}{3}\mu y\frac{\partial v}{\partial y} \\ K_c y\frac{\partial T}{\partial y} \end{pmatrix},$$

$$H_1 = \begin{pmatrix} 0 \\ -\frac{2}{3}\frac{\partial}{\partial x}(\mu v) \\ \epsilon p_1 - \frac{4}{3}\frac{\mu v}{y} + \frac{2}{3}\mu\frac{\partial u}{\partial x} - \frac{2}{3}v\frac{\partial \mu}{\partial y} \\ 0 \end{pmatrix}, \qquad H_2 = \begin{pmatrix} 0 \\ -\rho g y - \mu'\bar{J}_y\bar{H}_\theta \\ +\mu'\bar{J}_x\bar{H}_\theta \\ \mathbf{J}\cdot\mathbf{E}y \end{pmatrix}.$$

Here, ρ, u, v, p and T represent the density, x and y velocity components, the pressure and temperature, respectively. e is the total energy per unit volume and is given by $e = \rho C_v T + 1/2\rho\ (u^2 + v^2)$. The source terms are written as two vectors, H_1 and H_2. The vector H_1 contains the standard fluid dynamic source terms that arise because of the axisymmetric coordinates. The vector H_2 contains the source terms that arise from interactions with the electromagnetic radiation. These interaction terms are composed of the RMS values of the electric (E) and magnetic (H) fields and the electric current density (J). The energy equation contains the heat source from electromagnetic radiation given by $J \cdot E$. In the momentum equations, the source terms arising from buoyancy and the Lorentz forces (J x B) are included. At the present time, radiation losses from the plasma are not accounted for.

The numerical solution of Eqn. (1) is obtained by using Euler implicit discretization in time along with central differences in space for both the inviscid and viscous fluxes. Douglas-Gunn approximate factorization is used for the efficient solution of the resulting matrix operator. The solution procedure involves a block-tridiagonal inversion for each coordinate direction at each time (or iteration) step. The time-marching algorithm may be written in the following 'delta' form:

$$\left[\Gamma + \frac{\partial A}{\partial x} - \frac{\partial}{\partial x}R_{xx}\frac{\partial V}{\partial x}\right]\Gamma^{-1}\left[\Gamma + \frac{\partial B}{\partial y} - \frac{\partial}{\partial y}R_{yy}\frac{\partial V}{\partial y}\right]\Delta Q = -\mathcal{R}^n \qquad (2)$$

where R is the steady state version of Eqn. (1). Equation (2) ensures that the steady equation is satisfied as ΔQ tends to zero. The other terms in Eqn. (2) are defined as follows:

$$\Gamma = \frac{P}{\Delta t} - D$$

and the Jacobians A, B, D, R_{xx}, R_{yy} and V are defined as:

$$A = \frac{\partial E}{\partial Q}, \qquad B = \frac{\partial F}{\partial Q}, \qquad D = \frac{\partial H_1}{\partial Q},$$

$$R_{xx} = \frac{\partial E_v}{\partial Q_{vx}}, \qquad R_{yy} = \frac{\partial F_v}{\partial Q_{vy}}, \qquad V = \frac{\partial Q_v}{\partial Q}.$$

Here, Q_{vx} and Q_{vy} are the x and y derivatives of the viscous vector Q_v which is defined as:

$$Q_v = [0,\ u,\ v,\ T]^t.$$

In general, a small amount of fourth-order artificial dissipation is added to prevent odd-even splitting of the solution.

2.3 Maxwell Equation Solutions

The Maxwell equations for TM waves may be written in vector form analogous to the fluid dynamic equations:

$$\frac{\partial \tilde{Q}}{\partial t} + \frac{\partial \tilde{E}}{\partial x} + \frac{\partial \tilde{F}}{\partial y} = \tilde{H}, \qquad (3)$$

$$\tilde{Q} = \begin{pmatrix} H_\theta y \\ E_y y \\ E_x y \\ J_y y \\ J_x y \end{pmatrix}, \qquad \tilde{E} = \begin{pmatrix} (1/\mu')E_y y \\ (1/\epsilon)H_\theta y \\ 0 \\ 0 \\ 0 \end{pmatrix},$$

$$\tilde{F} = \begin{pmatrix} -(1/\mu')E_x y \\ 0 \\ -(1/\epsilon)H_\theta y \\ 0 \\ 0 \end{pmatrix}, \qquad \tilde{H} = \begin{pmatrix} -(1/\mu')E_x \\ -(1/\epsilon)J_y y \\ -(1/\epsilon)J_x y \\ (\sigma_{dc}E_y - J_y)\nu_c y \\ (\sigma_{dc}E_x - J_x)\nu_c y \end{pmatrix}.$$

In Eqn. (3), the first three rows represent the standard Maxwell's curl equations relating the magnetic field (H_θ) to the electric field (E_x and E_y). The last two equations are equations for the electric current density derived from momentum considerations for the conducting electrons in the plasma. The electrical properties of the medium, namely the electrical conductivity σ_{dc}, the collision frequency ν_c, the electrical permittivity ε and the magnetic permeability μ', are calculated.

The Maxwell equations are solved in the time domain by adopting an explicit time-marching procedure that is second-order accurate in time and space. The algorithm is similar to that conceived by Yee [4] and may be written as the following two-step procedure:

$$\tilde{Q}_h^{n+\frac{1}{2}} - \tilde{Q}_h^{n-\frac{1}{2}} = -2\Delta t\left(\frac{\partial \tilde{E}_e}{\partial x} + \frac{\partial \tilde{F}_e}{\partial y}\right)^n \tag{4a}$$

$$\left(1 + \frac{\sigma}{\epsilon}\Delta t\right)\left(\tilde{Q}_e^{n+1} - \tilde{Q}_e^n\right) = -2\Delta t\left[\left(\frac{\partial \tilde{E}_h}{\partial x} + \frac{\partial \tilde{F}_h}{\partial y}\right)^{n+\frac{1}{2}} - \tilde{H}^n\right] \tag{4b}$$

The subscript e refers to electric field components and the current densities and h refers to magnetic field components. The first step (Eqn. 4a) advances the magnetic field solution in time while the second step updates the electric field solution.

The above solution procedure yields an unsteady electromagnetic field. However, in terms of fluid time scales, the field is steady and is represented by the RMS values of the time varying components. In the coupled solution procedure, for each NS (Navier-Stokes) time step, we calculate the EM field over several cycles (between 1 and 10 cycles) and then time-average it to obtain the RMS field. Typically, more cycles were required per NS iteration step toward the start of the calculation. After about 100 iterations, it was generally sufficient to compute a single EM cycle per NS step. Because of the explicit nature of the Maxwell algorithm, the procedure was found to be fairly efficient. Details of the convergence of the algorithm and computer times were reported earlier.

2.4 Boundary Conditions

Inflow and outflow boundary conditions for both the fluid dynamic and the Maxwell equations are enforced by a vectorized implementation of the Method of Characteristics. An overview of the procedures is given below.

2.4.1 Boundary Conditions for the Navier-Stokes Equations

The fluid dynamic quantities on the boundaries are computed by combining Method of Characteristic procedures with physically realistic boundary conditions [5]. At the inflow boundary, the total pressure, the stagnation temperature and the flow angle are specified along with an upstream running characteristic. At the outflow boundary, the pressure is specified along with three outrunning characteristics. Symmetry and anti-symmetry conditions are enforced on the axis of symmetry, while no slip conditions, an appropriate temperature/heat flux boundary condition (as specified in the discussion) and the normal momentum equation are enforced on the walls. These boundary procedures proved to be very robust and provided physically realistic, well-behaved solutions at all boundaries.

2.4.2 Boundary Conditions for the Maxwell Equations

Boundary conditions for the Maxwell equations were likewise enforced by means of the Method of Characteristics. Maxwell's equations are a set of hyperbolic equations, and like any such set, they can be transformed to characteristic form by premultiplying the equations through by the modal matrix of the eigenvectors of the equation set. For the x-direction, we get:

$$\frac{\partial \hat{Q}_x}{\partial x} + \Lambda \frac{\partial \hat{Q}_x}{\partial x} + M_x^{-1}\tilde{B}M_x \frac{\partial \hat{Q}_x}{\partial y} = M_x^{-1}\tilde{H} \qquad (5)$$

where M_x^{-1} is the modal matrix for the x-direction, Λ is a diagonal matrix containing the eigenvalues of the system and $\hat{Q}_x$ is the characteristic vector in the x-direction that is defined as $Q_x = M_x^{-1}Q$ and is given by:

$$\hat{Q}_x = \begin{pmatrix} \frac{1}{2}(H_\theta + \sqrt{\frac{\epsilon}{\mu}}E_y)y \\ E_x y \\ \frac{1}{2}(H_\theta - \sqrt{\frac{\epsilon}{\mu}}E_y)y \end{pmatrix}.$$

The characteristic vector, $\hat{Q}$, contains the forward and backward traveling waves or the Riemann invariants of the system. The characteristic form of the equations is important for specifying boundary conditions particularly where the inlet waveguide feeds the microwave energy into the cavity. Here, the incoming characteristic represents the power that is input into the cavity (or the incident power) and has to be specified as a boundary condition. The outgoing characteristic represents the power that is reflected back by the load to the source. The value of this characteristic depends on the solution of the field in the cavity and the appropriate characteristic equation is used instead of a boundary condition. If characteristic variables are not used at boundaries, it becomes necessary to invoke an awkward iterative procedure to control the amount of power absorbed in the plasma, and it is impossible to distinguish incident power from reflected power so efficiency cannot be calculated.

The boundary conditions for the waveguide solutions deserve special mention. Previous research in the area of radio frequency plasma specified the tangential component of the electric field at the boundaries. While this is the physically correct boundary condition for a reflecting wall (where the tangential electric field is zero), it is not proper for the power inlet and outlet sections of the waveguide. This is because the value of the electric field at these boundaries depends on the amount of power dissipated in the plasma and cannot be known a priori. In an earlier paper, we showed that the correct quantities to keep fixed at these boundaries are the Riemann variable (or characteristic). At the inlet section, the forward running characteristic represents the incident power and is specified as a boundary boundary condition while the backward running characteristic represents the reflected power component and is calculated from the solution. At the exit section, the outgoing characteristic represents the power transmitted through the waveguide while the inward running characteristic represents any power that is incident at this end. Earlier, we discussed two kinds of conditions that may be applied at the exit of the waveguide -- transmitting and reflecting. For the waveguide with a transmitting exit condition, the inward running characteristic is zero. For the waveguide with a reflecting end wall at the exit, the inward running characteristic is equal to the negative of the outgoing characteristic (i.e., the transmitted power is reflected back toward the plasma).

The application of the locally one-dimensional Method of Characteristics yields the following expressions for the forward (+) and backward (-) running characteristics:

$$\hat{q}^{+} = \frac{1}{2}\,(E_y + Z_o H_\theta), \quad \hat{q}^{-} = \frac{1}{2}\,(E_y\; Z_o H_\theta) \tag{6}$$

where Z_o is the characteristic impedance given by $\sqrt{\mu'/\varepsilon}$.

As a check of our boundary procedure and to demonstrate the differences between the two undistorted electric fields, we plot the Maxwell solutions for a lossless waveguide in Fig. 3 for both transmitting and reflecting exit conditions. Figure 3a shows the RMS value of the axial electric field for the waveguide with a reflecting end wall. The characteristic equations yield the obvious condition $E_y = 0$ for this case. The result clearly shows a standing wave pattern in the waveguide. Since no power is dissipated in the waveguide, all the incident power is transmitted through to the end wall, where it is reflected back toward the microwave source. It is also evident that the exit wall acts as a node of maximum intensity. One-half wavelength upstream of the end wall is a second node of maximum intensity. As mentioned earlier, this node would serve as an ideal location for the plasma and good plasma stability is anticipated.

(We will show that this is indeed the case in the Results section of this paper.) In addition, the location of the waveguide end wall may be adjusted in order to fine tune the location of the plasma.

The waveguide with the transmitting end condition is shown in Fig. 3b. Surprisingly, this plot of the axial electric field again shows a standing wave pattern, although it is weaker than the standing wave in Fig. 3a. This means that not all of the incident power is transmitted through the exit section; rather, a percent of the power is reflected at this boundary (22% in this case). The reason for this is the use of locally one-dimensional Method of Characteristics at this (two-dimensional) boundary. For the axisymmetric waveguide, the one-dimensional boundary procedure cannot eliminate reflection completely. To specify this boundary condition correctly, it is necessary to employ the two-dimensional Method of Characteristics. In fact, this is a familiar problem in computational fluid dynamics and a formidable one. Fortunately, however, for microwaves traveling in a lossless waveguide, there is an exact solution. Using this exact solution, it becomes evident that the correct characteristic quantities are given by:

$$\hat{q}^{+} = \frac{1}{2}\,(E_y + Z_{TM}H_\theta), \qquad \hat{q}^{-} = \frac{1}{2}\,(E_y - Z_{TM}H_\theta) \tag{7}$$

where Z_{TM} is the characteristic impedance for TM waves in a waveguide and is given by $\sqrt{u'/\varepsilon - k^2/\omega^2\,\varepsilon^2}$. Here, ω is the frequency of the microwaves and k_c is the wavenumber in the radial direction.

Figure 3c shows the result for the transmitting waveguide using Eqn. (7). Now the field pattern is completely changed. The standing wave solution is no longer evident; instead, the field lines run parallel to the waveguide axis with the maximum occurring at the centerline. This is the correct solution for traveling waves in the waveguide. The power fluxes of the calculation also show that all the incident power is transmitted through the exit and none is reflected. It should also be noted that for this traveling wave solution there is no preferred axial location for the plasma; hence, the need for a stabilization device such as a bluff body is evident.

3.0 RESULTS

A summary of parametric results on the three microwave thruster configurations is presented in this section. We begin with the results on the bluff-body stabilized resonant plasma, then move to the free-floating resonant cavity plasmas and finally end with the waveguide plasmas.

3.1 Bluff-Body Stabilized Resonant Cavity Plasmas

The geometry for the configuration corresponding to the experimental results of Part 1 is given in Fig. 1b. A second geometrical configuration with a larger bluff body shape and a somewhat different flow geometry is given in Fig. 4. We begin with solutions for the larger bluff body (Fig. 4). First, we show a set of results for cold flow conditions to fix the details of the flowfield. Figure 5 shows the convergence rates for a sequence of cold flow calculations in the geometry of Fig. 5 for a series of Reynolds number conditions that more than cover the spectrum of the experimental measurements. Flowfield conditions for Reynolds numbers from 5 to 1000 have been computed. As the convergence rates show, convergence is good over all Reynolds number levels, with convergence of three to four orders of magnitude being obtained in 1000 iterations. Corresponding results for several of these cases are given in Fig. 6. At low speeds (low Reynolds numbers) the cold flow closes over the bluff body with no recirculation region, but as the speed (Reynolds number) is increased, a recirculation region develops that increases in length. This flowfield is representative of the undisturbed flow into which the microwave plasma is introduced. Of course, the plasma heating alters the flowfield dramatically.

Figure 7 shows the convergence of the combined Maxwell/Navier-Stokes equations for a representative case. As can be seen, convergence remains good when the plasma is present. We do, however, note that the process of finding an acceptable initial condition can be challenging, and the first solution in a sequence is generally found by a cut-and-try method. If a "hot" zone is not included in the initial condition, there will be no absorption. Just as in the experimental case, the initial condition must start with some "breakdown" region which must then be sustained to obtain power absorption.

The flowfield solution for a representative case is shown in Fig. 8. As can be seen, the plasma sits in the wake of the bluff body, but it causes a dramatic weakening in the size and strength of the recirculation zone, eventually leading to the complete removal of recirculation as is shown later. These calculations are for the TM011 mode, and the plasma forms at the lower node. The bluff body has been situated so that the wake region corresponds with this node.

The temperature contours for a series of different microwave powers are shown on Fig. 9. As the power is increased the plasma increases in length, but the radial growth is restricted by the size of the bluff body. The experimental measurements have shown similar changes in the plasma shape with increases in the power. We also note that increased heat addition causes a decrease in the recirculation region, eventually almost eliminating it at the higher (4 kW) power level.

Similar temperature contour plots showing the effect of pressure level are given on Fig. 10. Increases in pressure cause diffusion to become smaller so that the recirculation region becomes stronger. Increased pressures also lead to stronger effects of buoyancy which act in a direction to augment this. The plasma also becomes notably more compact at the higher pressures, again in agreement with qualitative observations obtained from the experiments.

Representative calculations for the experimental geometry of Fig. 1b are presented in Fig. 11. For this case, the flow is accelerated through an orifice in the bottom of the chamber duplicating the experimental setup. Representative temperature contours and streamlines are given on Fig. 11. Note that in this case, there is no recirculation in the base region, although there is a weak recirculation cell in the base of the bulb region where the narrow orifice creates a "dead-water" region. The peak temperatures for this case are about 11,500 K, a value that is in good agreement with experiment. Again, the plasma size is restricted by the size of the bluff body, so the present plasma is quite narrow in size. Larger bluff body sizes (and the increased plasma diameters) enable more microwave energy to be added to the flow so that the average temperature of the heated gas increases, thus providing higher propulsive performance. The plasma shape noted here is similar to that observed in the experiments. Quantitative comparisons of the shapes is planned, but the data from the experiments has not been reduced as yet.

A comparison between the predictions and the experiments for the bluff-body stabilized plasma is given in Figs. 12 and 13. Figure 12 shows the variation of the coupling efficiency with changes in the mass flow rate at two power levels, 1 and 2 kW. Coupling efficiency is here defined as the ratio of the power absorbed to the incident power. Losses include only the reflected power, a quantity that is small because of the use of a cavity standing wave. The predictions are in excellent agreement with the measurements for both power levels. Similar comparisons of the peak temperatures are given in Fig. 13. The comparison is again very good and, further, we note that the smaller bluff body provides nearly a 2000 K temperature rise as compared to the larger one. The subject experimental measurements were considered questionable because they were so high, especially as compared to the free-floating plasma, but the present calculations show that a higher temperature is justified because of the size of the bluff body. The larger bluff body provides peak temperatures that are more in line with previously observed microwave plasmas, but it also shows that it is possible to obtain control over the peak temperature.

3.2 Results for the Free-Floating Resonant Cavity Plasma

The geometrical configuration for the free-floating resonant cavity plasma is given in Fig. 1a. Here we show the cavity, the sphere-cylinder flow tube, and the undistorted microwave field in the TM012 mode. The initial results for the free-floating plasma (Fig. 14) show the placement of the plasma occurs in the center of the sphere at the middle node of the undisturbed E-M field in agreement with experimental observations. The predictions indicate that the conditions chosen for the experiments lie near a boundary which differentiates between the existence of and the absence of a recirculating region in the sphere, but that, in general, the experiments are run just above this boundary so that recirculation is not observed. The field lines for the absorbing electric field are given on Fig. 15. Note by comparison with Fig. 1a, the substantial amount of distortion that is observed. Clearly, the prediction of the plasma requires a coupled Maxwell/Navier-Stokes solution. The distorted electric field also gives clear evidence of the "skin effect" that concentrates the field at the surface of the plasma and leaves the interior of the plasma nearly constant.

The effect of microwave power on the shape and location of a free-floating plasma in a straight cylindrical duct is given on Fig. 16. For a series of input powers starting at low powers, the plasma forms at the bottom of the three nodes in the TM012 mode, and continues to grow in size as the power is increased from 1.5 to 2 kW. At the 3 kW, the plasma begins to expand above the lowest node and to absorb a small fraction of the radiation in the middle node, and at 4 kW it jumps to the top and middle nodes. Using this 4 kW solution as the initial condition for first a 3 kW and then a 2 kW calculation, the power in the plasma is absorbed from the middle node of the standing wave. These results show that the location of the plasma in a straight tube depends upon the initial condition, i.e., it depends upon the manner in which the plasma was initiated. No experimental results are available for a straight cylindrical tube, so no verification of this multiplicity of plasma locations has been shown, but the expansion of the plasma at higher powers to cover two nodes has been observed experimentally. Similar calculations for the sphere-cylinder tube in Fig. 17 show the plasma forms at the center node and expands in size with increasing input power in agreement with experiment. These results which are chosen to match the experimental results described in Part I, show that the flowfield in the spherical region contains a large recirculation region at the lower power levels, but that this recirculation is weakened as the power is increased, and eventually is eliminated at the 4 kW case. These sphere-cylinder results also show the plasma size expands to form a double plasma at the higher powers, in agreement with the experiments.

The effects of increasing the inlet gas velocity from 0.1 to 1 m/s are shown in Figs. 18 and 19 for the sphere-cylinder geometry and the straight cylindrical geometry, respectively. In both cases, the higher inlet velocities displace the plasma downward away from the incoming flow. The higher inlet velocities reduce the upward diffusion of the heat and indicate the location of the energy absorption regions more directly. For both geometries, the effect of buoyancy is more pronounced at the lower velocities where recirculation is observed, while at the higher velocities, the recirculation region is no longer present. Corresponding effects of changing the pressure on both the sphere-cylinder and the straight cylinder are shown in Figs. 20 and 21. As for the bluff-body stabilized plasma, the larger plasmas reduce the size of the plasma making it more compact. Experimental measurements have also noted this size change with increases in the pressure level. The increased pressure also increases the size of the recirculation region because the increased pressure decreases the rate of diffusion causing diffusive effects to become more significant relative to buoyancy.

Some direct comparisons with experiment are given in Figs. 22 and 23. Figure 22 shows the predicted and measured peak temperatures as a function of the pressure. Again, the peak temperature is nearly independent of mass flow for both the predictions and the measurements. The predictions are some 1000 K lower than the measurements, but the difference between the present free-floating plasma and the previously discussed bluff-body stabilized plasma is well predicted by the analysis. The predicted coupling efficiencies for the free-floating plasma are given in Fig. 23, and show that the free-floating plasma is capable of coupling almost all of the incident energy into the plasma. There is some fall-off in efficiency predicted at the lowest and higher pressures. The reason for this is that the present cavity incorporates a sliding short that can be used to re-tune the cavity length in the presence of losses (absorption). The experimental measurements of efficiency are considerably lower than the predictions because they include heat losses to the wall and electromagnetic losses through the wall. The experiments were, however, conducted in such a way that the sliding short was adjusted in the presence of the plasma until the reflected power was zero, or nearly so, indicating the true coupling efficiency was nearly 1000%, in agreement with the predictions.

3.3 Results for the Bluff-Body Stabilized Plasma in a Waveguide

3.3.1 Representative Waveguide Solution

To provide a physical picture of waveguide heated plasmas, a typical solution for the waveguide with a transmitting boundary is shown in Fig. 24. The flowfield solution is given in Fig. 24a and the electric field solution is in Fig. 24b. For this case, the inlet gas velocity is 3 m/s and the gas pressure is 1 atm; the corresponding mass flow rate is 1.1 g/s. The incident microwave power is 3.5 kW, while the diameter of the bluff body used to hold the plasma is 4.5 cm.

The temperature contours in Fig. 24a show that the plasma discharge is maintained in the wake of the bluff body. As shown in Fig. 3, the electric field in the transmitting waveguide does not offer any preferred location for the plasma so the location of the plasma is determined purely by the dynamics of the flow. The fluid dynamics tends to push the plasma downstream while the microwave power pulls it upstream. The plasma is stable in a region where these two forces balance out. The plasma is long and slender with its outer diameter being defined by the edge of the bluff body. This is because of high local gas velocities at the outer edge of the bluff body. The peak plasma temperature occurs on the central axis and is about 9150 K which is typical of helium plasmas of this size. The streamline contours show evidence of a recirculating region in the wake of the bluff body, however, the recirculating region is quite weak relative to its cold flow counterpart under similar conditions. This is because the strong heat addition in the plasma tends to suppress the recirculation zone. In fact, in some cases, the recirculation is totally eliminated.

The axial and radial electric field contours are shown in Fig. 24b. The electric field lines are seen to be strongly distorted in the presence of the plasma (compare with Fig. 3). Because of the skin effect, the absorption of the energy occurs at the surface (or skin) of the plasma. Consequently, strong electric field gradients exist on the surface while the electric field is zero inside the plasma. Of the 3.5 kW that is incident on the plasma, 2.4 kW is absorbed by the plasma, 1 kW is reflected back toward the inlet and 0.1 kW is transmitted through the waveguide exit. The coupling efficiency, which is the ratio of absorbed to incident power, is 70% for this case. In Fig. 24b, the power reflected by the plasma creates a standing wave pattern upstream of the plasma. Downstream of the plasma, the electric field lines run parallel to the waveguide axis, representing the transmitted component. For the transmitting waveguide configuration, both the reflected and transmitted powers are lost from the system.

3.3.2 Comparison of Transmitting and Reflecting Waveguides

In a reflecting waveguide, the power transmitted to the exit section is reflected back toward the plasma and thus gets a second chance at being absorbed. It is interesting to check if this alternate configuration gives better energy coupling than the transmitting waveguide. Figure 25 shows the results for a reflecting waveguide for the same conditions used in Fig. 24.

The reflecting waveguide solution in Fig. 25 is remarkably similar to the transmitting waveguide solution. The peak temperature is now 9310 K while the coupling efficiency is 68%. The streamlines, not shown, are also qualitatively similar. The electric field solution now shows evidence of a standing wave pattern downstream of the plasma as well (indicating power reflection at the exit). However, the reflecting condition has made very little impact on the nature of the plasma. One reason for this may be that only a small amount of power is transmitted through the plasma in this case.

Figure 26 compares the performance of the reflecting and transmitting waveguides over a wide range of powers; the reflecting waveguide results are shown on the top (Figs. 26a to 26d) while the transmitting waveguide results are shown on the bottom (Figs. 26e and 26f). The flow conditions are once again the same as before (1 atm and 3 m/s inlet velocity). For the reflecting waveguide (Figs. 26a to 26d), the plasma is maintained stably in the wake of the bluff body over the range of powers. As the power is reduced from 5 kW to 1 kW, the plasma shrinks in size. This effect is more noticeable in the plasma length than in its radius because the bluff body restricts the radial size of the plasma. The peak plasma temperature, however, stays constant at about 9300 K. Of particular interest is the double plasma that is starting to form at the 5 kW condition. Such double plasmas have also been observed experimentally. When the power is reduced below 1 kW, the plasma is eventually extinguished. Such a power threshold exists because, at low powers, the electrons start recombining more rapidly than they are created by ionization. In this case, this minimum power was about 800 W, which is similar to experimental values.

An interesting observation for the reflecting waveguide is that the coupling efficiency of the plasma increases as the power is reduced, starting from 58% (at 5 kW) to 95% (at 1 kW). This is probably because at high powers the plasma elongates in size but is restrained from growing radially by the bluff body. As a result, the plasma reflects more at higher powers and absorbs less. This result is quite different from the results for free-floating resonant cavity plasmas where coupling efficiencies up to 100% are obtainable at all power levels.

The transmitting waveguide results for similar conditions are shown in Figs. 26e and 26f. At the higher powers (5 kW and 3.5 kW), the plasma discharge is qualitatively similar to the reflecting waveguide plasma. But at powers lower than about 3 kW, it was impossible to maintain a stable plasma. This is because at these lower powers, the convection dynamics of the flow dominates over the microwave power and blows the plasma away from the wake of the bluff body. In other words, the mass flow rate associated with the plasma is higher than the plasma propagation speed at this condition. Thus, the transmitting waveguide can maintain stable plasmas only above this power threshold of 3 kW. Of course, for lower gas flow rates, this threshold would be lowered; but, for the flow rates of interest here, no significant change in the threshold power was observed. Therefore, the reflecting waveguide configuration can maintain stable plasmas over a wider range of powers than the transmitting waveguide.

The improved performance of the reflecting waveguide arises because it absorbs energy in the standing wave mode while the transmitting waveguide absorbs in the propagating wave mode. For the propagating mode, the electric field contours do not provide a preferred location for the plasma, while, for the standing wave mode, the nodes of maximum field intensity do provide such a location. For the reflecting end wall, one such node occurs one-half wavelength upstream of the end wall. The combined presence of this node and the wake of the bluff body contributes to increased stability of the plasma over a wide range of input powers. In fact, experiments have indicated that it is sometimes possible to maintain the plasma even in the absence of the bluff body. For the parametric studies in the rest of this report, we concentrate on the reflecting configuration.

3.3.3 Location of the Plasma

The location of the plasma in the reflecting waveguide is influenced by the location of the maximum node. Thus, by adjusting the location of the reflecting end wall, it should be possible to control the precise location of the plasma. Figure 27 shows the results when the reflecting end wall is positioned at two different downstream locations — in Fig. 27a, the distance between the base of the bluff body and the end wall is 3 D_b (where D_b is the bluff body diameter); while, in Fig. 27b, this separation distance is 4 D_b. In Fig. 27a, the plasma is pushed up against the bluff body, while in Fig. 27b, the plasma is detached from the bluff body. Clearly, this movement of the plasma is caused by the migration of the maximum node as the end wall is moved further downstream.

The streamline contours for the two conditions are also shown in Fig. 27. The recirculation region is seen to grow as the plasma is moved downstream of the bluff body. The heat transfer to the bluff body is influenced by the strength of this recirculating region. In Fig. 27a, the heat conducted from the plasma to the bluff body is quite high (0.46 kW, corresponding to about 15% of the incident power). In Fig. 27b, the heat loss to the bluff body is only 0.04 kW (or 1.3% of the incident power). The condition in Fig. 27a is clearly undesirable. The high heat loss to the bluff body results in poor energy conservation and low overall thermal efficiency. Furthermore, high heat load may also result in degradation of the material of the bluff body. Thus, the control of the plasma location that is made possible with the reflecting waveguide can ensure better overall performance.

3.3.4 Effect of Bluff Body Size

We observed in Fig. 24 that the radius of the plasma was defined by the size of the bluff body. It is interesting then to see how the plasma characteristics change when a smaller bluff body is employed. Figure 28 shows the temperature contours and streamlines for a plasma (incident power = 3 kW, 1 atm pressure, 3 m/s inlet velocity) that is stabilized by a 2 cm diameter bluff body. The peak plasma temperature is now significantly higher at about 11,600 K. This higher temperature is a consequence of the smaller size of the plasma. Such an effect has been previously observed both experimentally and theoretically. This temperature is also in agreement with earlier measurements of waveguide plasmas, which employed a bluff body of similar size. Furthermore, the temperature contours show the plasma very closely attached to the base of the bluff body. The streamline contours show no evidence of recirculation in the wake indicating that the high heat addition rate in this region has completely suppressed it.

The coupling efficiency for this calculation is 47% compared to about 68% for the 4.5 cm bluff body. It is evident that the size of the plasma restricts its absorption capacity and causes a large portion of the incident power to be reflected back. As in the earlier case, the size of the bluff body controls the radial extent of the plasma and, therefore, plays a crucial role in determining the efficiency of energy coupling. In addition, there is also considerable heat loss to the bluff body because of the close proximity of the plasma to the bluff body (0.22 kW or 7% of the incident power) resulting in high heat loads to the bluff body as well. This heating could again be controlled by fixing the location of the bluff body with respect to the standing wave mode.

We have established some of the basic characteristics of plasmas heated in a waveguide configuration. In the remainder of the report, we carry out detailed parametric studies to establish how the plasma characteristics change under different operating conditions. The plasma characteristics examined are the size of the plasma (length and width), the size of the recirculation region, the coupling and thermal efficiencies of the plasma and, finally, the peak and average gas temperatures. The results, summarized in Figs. 29 to 33, are plotted against the mass flow rate of helium. Mass flow rate may be varied two ways — by changing the inlet gas velocity and by changing the gas pressure. We consider both these effects independently. Further, the results are presented for two incident power levels (2 kW and 4 kW). Finally, in addition to the results for the 4.5 cm bluff body, some results are shown for the smaller bluff body size (2 cm diameter) as well.

Similar parametric studies are currently being performed experimentally with the apparatus shown in Fig. 2. At the present time, very little consolidated data are available for direct comparison. Earlier experiments for a smaller flow geometry and a rectangular waveguide have yielded plasma temperatures of 12,000 K and coupling efficiencies of 60 to 80%; these data are in qualitative agreement with the present results. In addition, many of the trends predicted computationally have been corroborated experimentally.

3.3.5 Size of the Plasma

The size of the plasma is, naturally, of importance. We have already seen that the size of the plasma influences the coupling efficiency of the plasma. Furthermore, the heat loads on the walls and on the bluff body also depend on plasma size. Figure 29 shows the plasma length and the mean plasma diameter plotted against mass flow rate. Both quantities are normalized with respect to the size of the bluff body. Four sets of data are shown. Here, as well as in Figs. 30 to 33, the circles represent the case where the mass flow rate is varied by changing the gas velocity (2 kW power, 1 atm pressure); the triangles are for a higher power of 4 kW, 1 atm pressure and different velocities; the squares are again for the lower power of 2 kW with the gas velocity maintained at 0.75 m/s while gas pressure is varied; and finally, the stars show the calculations for the 2 cm bluff body for two gas velocities (1 atm pressure, 3 kW power).

The most noticeable effect in Fig. 29 is the increase in the size of the plasma with power. The 4 kW plasmas are seen to be significantly longer (by about 50%) and somewhat wider (by about 20%) than the 2 kW plasmas. As noted earlier, the restriction in radial growth is due to the presence of the bluff body. Increasing the gas velocity reduces the size of the plasma slightly in most cases (except the length of the 4 kW plasma which grows somewhat). This is a Reynolds number effect — higher gas velocities mean higher Reynolds number and, hence, less diffusion of thermal energy. The plasma thus becomes more compact at higher velocities. Increasing pressure also increases the Reynolds number and a slight reduction in plasma size is evident. The results for the smaller bluff body show similar plasma sizes with respect to the smaller diameter. In terms of actual size, these plasmas are thinner and about half as long as the 4.5 cm bluff body plasmas.

3.3.6 Size of the Recirculation Region

Figure 30 shows the variation in the length of the recirculating zone in the wake of the bluff body. As mentioned earlier, the recirculating zone influences the rate of heat transfer to the bluff body. Depending on the exact location of the plasma with respect to the bluff body, the size of the recirculation zone varies and so does the heat transferred to the bluff body. When the plasma is in close proximity to the base of the body, the recirculation region is totally suppressed (as in Fig. 28) and there is a significant heat load on the bluff body. Figure 30 shows that the recirculation region is suppressed at low flow velocities and low pressures, that is, at low mass flow rates. Increasing the mass flow rate by increasing gas velocity or pressure elongates the recirculating region (the effect of pressure is slightly greater). This is again a Reynolds number effect. At low Reynolds numbers, diffusion of thermal energy is significant and the temperature contours extend over a larger region around the plasma; the larger this region, the more recirculation is suppressed. Also, Fig. 30 shows that at higher powers the recirculating region is suppressed over a bigger range of mass flows (or Reynolds numbers). Clearly, at higher powers the intensity of heat addition is greater and the plasma is bigger, both of which result in a stronger suppression of recirculation.

3.3.7 Coupling Efficiency

The coupling efficiency of the plasma is defined as the percent of the incident power that is absorbed by the plasma. Figure 31 shows the coupling efficiency plotted against mass flow rate. There appears to be very little dependence on the flow rate. For the 2 kW plasma, coupling efficiencies are about 80% while for the 4 kW plasma, they are about 65 to 70%. The lower coupling efficiencies at higher powers was noted earlier and may be attributed to the restriction in the radial growth of the plasma by the bluff body. This also explains why the coupling efficiencies for the 2 cm bluff body plasmas (3 kW) are less than 50%.

3.3.8 Overall Thermal Efficiency

Once the plasma absorbs the radiation, it loses energy to the surroundings by conduction and radiation. It is, therefore, important to check how much of the energy is actually retained by the gas. The overall thermal efficiency is defined as the total energy in the gas at the exit section of the flow tube divided by the incident power.

By definition, it will be less than the coupling efficiency by exactly the amount of energy that is lost to the side walls and the bluff body. Figure 32 presents the overall thermal efficiency versus mass flow rate. Increasing mass flow rate (either by increasing pressure or flow velocity) increases Reynolds number, decreases thermal diffusion, reduces plasma size, increases the size of the recirculation region and thereby increases the thermal efficiency. The overall efficiency is also seen to be higher for the 2 kW plasma than for the 4 kW plasma. This is clearly because of the larger size of the 4 kW plasma. Figure 32 also shows that, at high enough flow rates, it is possible to achieve thermal efficiencies up to 75%, which is nearly equal to the coupling efficiency for those cases. Under these conditions, practically all diffusion losses are eliminated. There is, however, a price to pay for this as will be evident in the next section.

3.3.9 Gas Temperatures

It is important to ensure that the incident radiation is absorbed efficiently and retained by the gas. It is also important to check how much the gas is heated by the radiation. It is the latter factor that determines the performance of the thruster device (the higher the gas temperature, the higher the thrust and specific impulse of the thruster). Figure 33 presents both the peak gas temperature that occurs in the central core of the plasma and the average gas temperature at the exit of the flow tube. The peak gas temperature is a useful parameter for characterizing plasmas, especially since this is what is measured most frequently in experiments. The average temperature is, however, more important since it determines the performance of the thruster. Figure 33 shows that peak temperatures are around 9000 to 10,000 K for the 4.5 cm bluff body and about 11,500 K for the 2 cm bluff body. The peak temperature is relatively insensitive to flow conditions; but a slight increase is noticed with increasing gas flow rate. This latter effect may be explained by the slight reduction in plasma size at higher flow rates.

The average temperatures in Fig. 33 are seen to be considerably less than the peak temperatures. They range from about 2200 K at low flow rates to about 1200 K at high flow rates. Further, the 4 kW plasma shows a slightly higher mean temperature throughout. Thus, better performance is possible at low mass flow rates, but the overall thermal efficiencies are poor; whereas at high mass flow rates, thermal efficiencies are high but the performance is lower. Clearly, a compromise has to be made between these two opposing requirements. A similar situation exists with regard to power. Higher powers mean better performance but, as seen in Figs. 31 and 32, high powers are also less efficient.

Finally, to get an idea of what level of performance these temperatures promise, we calculate the I_{sp} (specific impulse) using simple one-dimensional expansion to vacuum. Corresponding to a temperature of 2200 K, the I_{sp} is 480 s while at the lower temperature of 1200 K, the I_{sp} is 350 s. These performance numbers are in the range that current chemical systems can provide. Clearly, the feasibility of waveguide heated propulsion and of microwave propulsion, in general, depends on whether higher performance can be attained. This will be an important aspect of microwave propulsion research in the next few years.

4.0 SUMMARY

A detailed analytical study of microwave propulsion has been undertaken. The absorption and flowfield characteristics of three different microwave absorption configurations — free-floating plasma in resonant cavities, bluff-body stabilized plasmas in resonant cavities, and bluff-body stabilized plasmas in waveguides — have been included. Results have been compared with experimental measurements both qualitatively and quantitatively. In general, the model correctly predicts the shape, size and location of the plasma, and its response to increases in microwave power, changes in the pressure, the plasma movement with changes in the flow velocity, and the expansion of the single plasma to a double plasma in several limiting conditions.

In terms of quantitative comparisons, the model properly predicts the peak temperature in the plasma for the various geometric configurations tested. Of particular interest here is the fact that even though the peak temperature is nearly constant for any one configuration, the model correctly predicts the differences in peak temperatures that have been observed experimentally between geometrical configurations. In particular, experimental measurements of the peak temperatures in free-floating plasmas were in good agreement with previous microwave plasma temperature measurements by other investigators, but the measurements in bluff-body stabilized plasmas had shown peak temperatures that were considerably higher than these well-established levels. Consequently, it had been thought that they were in error. The predictions, however, show that the peak temperature in bluff-body stabilized plasmas increases substantially as the body size is decreased, and predict values in close agreement with the experiments for the same sized bluff bodies. In addition to the temperature comparisons, the predicted coupling efficiencies are in good agreement with the experimental measurements also. Finally, predictions of the low power threshold for maintaining a plasma are well-predicted for all three geometries.

The predictions indicate that the experimental conditions have all been run at conditions that are near the boundary in which buoyancy-induced recirculation is observed in the plasma. In the flow ranges of the experiments, small changes can lead to strong recirculation, or can remove the recirculating region entirely, depending on the pressure and velocity levels. Computations with and without gravitational effects included show, however, that the plasmas are not strongly affected by this recirculation, so that the experimental results are not suspect because they are conducted near this boundary. The analytical results also show that the presence of the plasma with its strong heating characteristics can reduce or even remove the familiar recirculation region that occurs behind bluff bodies, but that they continue to serve effectively as "flame-holders".

A major shortcoming of the microwave plasma experiments that have been made to date is that although they have all shown high peak temperatures, the average gas temperatures have been quite low. These small mean temperature rises, seldom more than a few hundred Kelvins, strongly limit the expected specific impulse provided by potential microwave thermal thrusters. The parametric studies based on the model suggest ways for increasing average temperature to values that will produce attractive specific impulses. For the bluff-body stabilized plasmas, the average temperature increases rapidly as the size of the bluff body is increased. The reason is that the bluff-body size sets the diameter of the plasma, as well as the amount of mass flow that goes through the plasma. Similarly, in the free-floating plasma, the fraction of fluid that flows through the plasma can be increased by carefully controlling the tube diameter, its shape, and the mass flow. Such optimizations are best made analytically to be able to identify the regimes in which experimental demonstrations should be made, while still keeping the plasma sufficiently far from the wall to prevent arcing. Additional research in this area is needed to demonstrate nominal upper bound temperature measurements that can be obtained with microwave plasmas to properly define their practical ranges of specific impulse.

The other major limitation of microwave thrusters is the maximum thrust size limitation set by the wavelength of the microwaves. The wavelength inherently sets the size of the plasma, and, hence, the nominal thrust level because absorption is most effectively limited to resonant cavity absorption. Waveguide absorption has been demonstrated herein, but it is not as efficient (in terms of coupling efficiencies) as resonant cavity stabilized plasmas. Waveguide plasmas reflect substantial fractions of the incident power back to the load where they are lost and, in addition, they promise little in terms of increased thrust levels. Because of these size limitations, it is impossible to heat large quantities of gas in a microwave thruster, so that even though high power microwave sources can be built in lightweight form, they cannot be used directly to scale up the thrust sizes available with microwave thrusters. Specific efforts directed toward this scaleup process have never been attempted and conceptual studies, using the available analytical and experimental tools described herein, would appear to be a second promising area for further research.

5.0 REFERENCES

[1] Boulos, M. I., "Flow and Temperature Fields in the Fire-Ball of an Inductively Coupled Plasma", IEEE Trans. Plasma Science, Vol. PS-4, No. 1, 1976, pp. 28-39.

[2] Wei, D., Apelian, D., and Farouk, B., "Effects of Coil Location and Injection Flow Rate in an Inductively Coupled Plasma Torch", AIAA Paper 85-1634, July, 1985.

[3] Rhodes, R., and Keefer, D. R., "Numerical Modelling of a Radio Frequency Plasma in Argon", AIAA Journal, Vol. 27, No. 12, Dec. 1989, pp. 1779-1784.

[4] Yee, K. S., "Numerical Solution of Initial Boundary Value Problems Involving the Maxwell Equations in Isotropic Media", IEEE Transactions on Antennas and Propagation, AP-14, May 1966, pp. 302-307.

[5] Merkle, C. L. and Choi, Y.-H., "Computation of Low-Speed Flow with Heat Addition", AIAA Journal, Vol. 25, No. 6, June 1987, pp. 831-838.

6.0 A CUMULATIVE CHRONOLOGICAL LIST OF WRITTEN PUBLICATIONS

1. Venkateswaran, S., Thynell, S. T., and Merkle, C. L., "A Study of Thermal Radiation Transfer in a Solar Thruster", ASME Proceedings-1990, AIAA/ASME Thermophysics and Heat Transfer Conference, HPD-Volume 137, pp. 125-132, 1990.

2. Choi, Y.-H., "Computation of Low Mach Number Compressible Flow", Ph.D. Thesis in Mechanical Engineering, The Pennsylvania State University, May 1989.

3. Venkateswaran, S., Merkle, C. L. and Thynell, S., "An Analysis of Direct Solar Thermal Rocket Propulsion", AIAA Paper No. 90-0136, AIAA 28th Aerospace Sciences Meeting, January 8-11, 1990, Reno, NV.

4. Venkateswaran, S., Merkle, C. L. and Micci, M. M., "Analytical Modeling of Microwave Absorption in a Flowing Gas", AIAA Paper 90-1611, AIAA 21st Fluid Dynamics, Plasma Dynamics and Lasers Conference, June 18-20, 1990, Seattle, WA.

5. Venkateswaran, S., "Analysis of Solar and Microwave Thermal Propulsion Systems", Ph.D. Thesis, The Pennsylvania State University, May 1991.

6. Venkateswaran, S. and Merkle, C. L., "Numerical Investigation of Bluff Body Stabilized Microwave Plasmas", AIAA Paper No. 91-1503, AIAA 22nd Fluid Dynamics, Plasma Dynamics and Lasers Conference, June 24-26, 1991, Honolulu, HA.

7. Venkateswaran, S. and Merkle, C. L., "Numerical Modelling of Waveguide Heated Microwave Plasmas", accepted for inclusion into the Symposium on Multi-Disciplinary Applications of CFD, ASME Winter Annual Meeting, 1991, Atlanta, GA.

8. Venkateswaran, S., Merkle, C. L. and Thynell, S. T., "An Analysis of Direct Solar Thermal Rocket Propulsion", Journal of Propulsion and Power, accepted for publication.

9. Venkateswaran, S., Thynell, S. T., and Merkle, C. L., "A Study of Thermal Radiation Transfer in a Solar Thruster", Journal of Heat Transfer, accepted for publication.

10. Venkateswaran, S. and Merkle, C. L., "Coupled Navier-Stokes Maxwell Solutions for Microwave Propulsion", K. W. Morton, Ed., Lecture Notes in Physics, Proceedings from the 12th International Conference on Numerical Methods in Fluid Dynamics, published by Springer-Verlag, 1990, pp. 475-479.

7.0 PROFESSIONAL PERSONNEL ASSOCIATED WITH RESEARCH EFFORT

Professional Staff —

Charles L. Merkle, Principal Investigator, Distinguished Alumni Professor, Mechanical Engineering.

Yun-Ho Choi, Ph.D., January 1985-April 1989. Ph.D. Thesis title, "Computation of Low Mach Number Flowfields with Strong Heat Addition". Present position: Research Scientist, Sverdrup, Inc., NASA/Lewis Research Center, Cleveland, Ohio.

Graduate Students —

Sankaran Venkateswaran, Graduate Assistant, September 1985-January 1991. Ph.D. Thesis title, "Analysis of Solar and Microwave Thermal Propulsion Systems". Present position: Research Associate, Propulsion Engineering Research Center, The Pennsylvania State University.

8.0 INTERACTIONS/SPOKEN PRESENTATIONS

Venkateswaran, S., Merkle, C. L. and Thynell, S., "Analysis of Direct Solar Thermal Rocket Propulsion", AIAA Paper No. 90-0136, AIAA 28th Aerospace Sciences Meeting, January 8-11, 1990, Reno, NV.

Venkateswaran, S., Merkle, C. L. and Micci, M. M., "Analytical Modeling of Microwave Absorption in a Flowing Gas", AIAA Paper No. 90-1611, AIAA 21st Fluid Dynamics, Plasma Dynamics and Lasers Conference, June 18-20, 1990, Seattle, WA.

Venkateswaran, S. and Merkle, C. L., "Numerical Investigation of Bluff Body Stabilized Microwave Plasmas", AIAA Paper No. 91-1503, AIAA 22nd Fluid Dynamics, Plasma Dynamics and Lasers Conference, June 24-26, 1991, Honolulu, HA.

Venkateswaran, S. and Merkle, C. L., "Numerical Modelling of Waveguide Heated Microwave Plasmas", accepted for inclusion in the 1991 ASME Winter Annual Meeting, Atlanta, GA.

Venkateswaran, S. and Merkle, C. L., "Coupled Maxwell/Navier-Stokes Solutions for Microwave Propulsion", accepted for inclusion to the 4th International Symposium on Computational Fluid Dynamics, University of California at Irvine, September 1991.

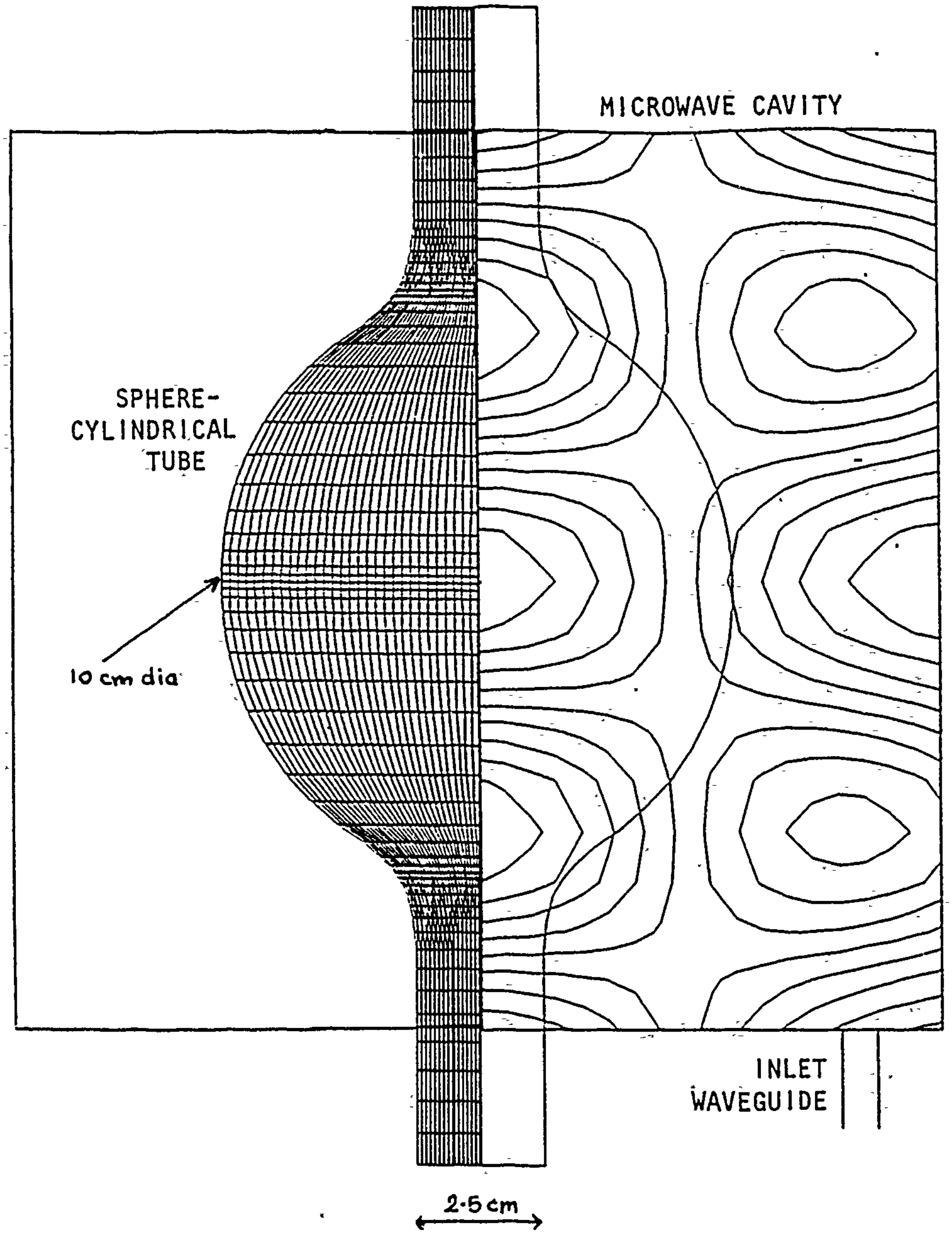

Figure 1a. Fluid dynamic grid for sphere-cylindrical tube with the microwave cavity. Right side of the cavity shows the no-loss field pattern of the TM_{012} mode.

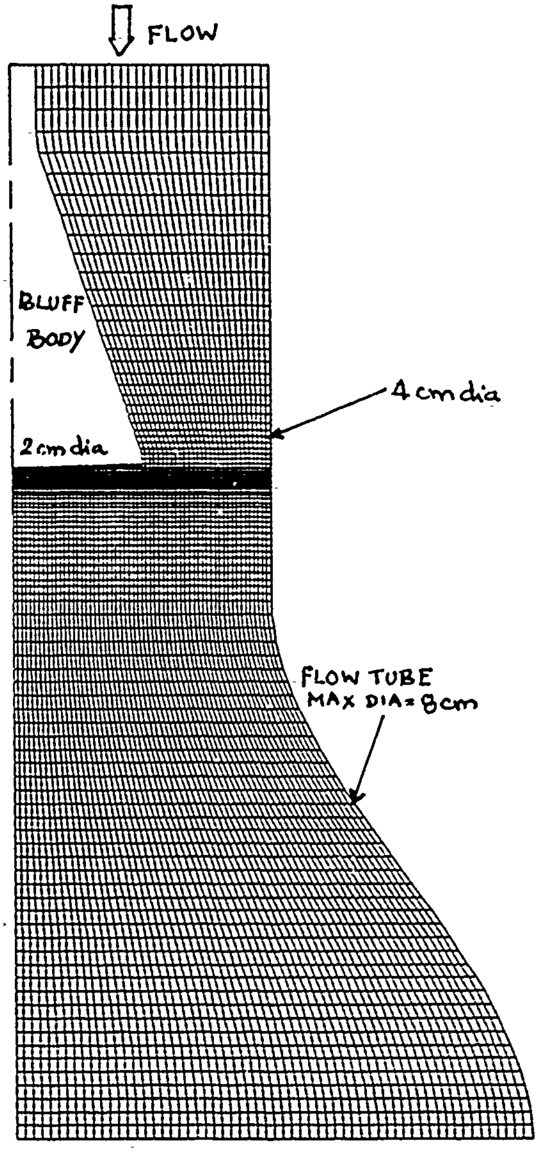

Figure 1b. Geometry for bluff-body stabilized resonant cavity.

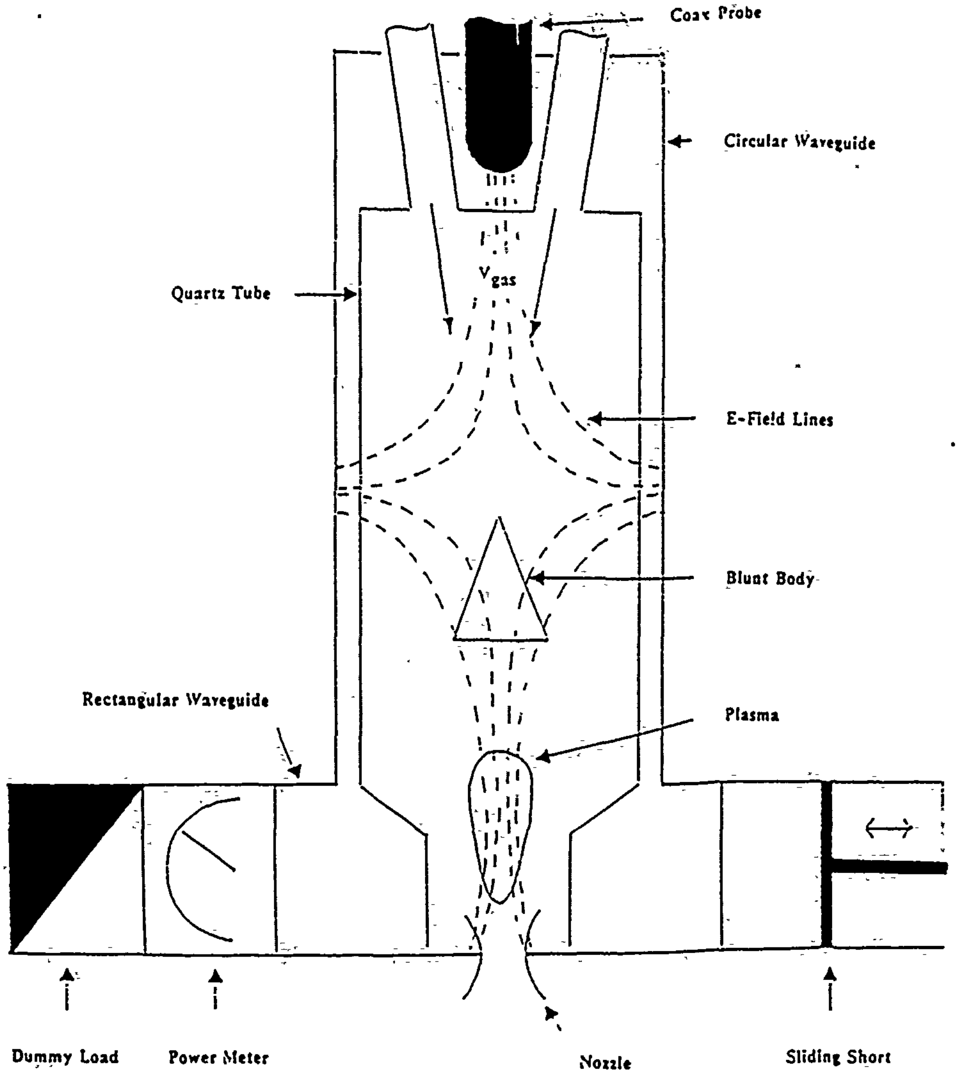

Figure 2. Schematic of experimental set-up for plasmas generated in a circular waveguide .

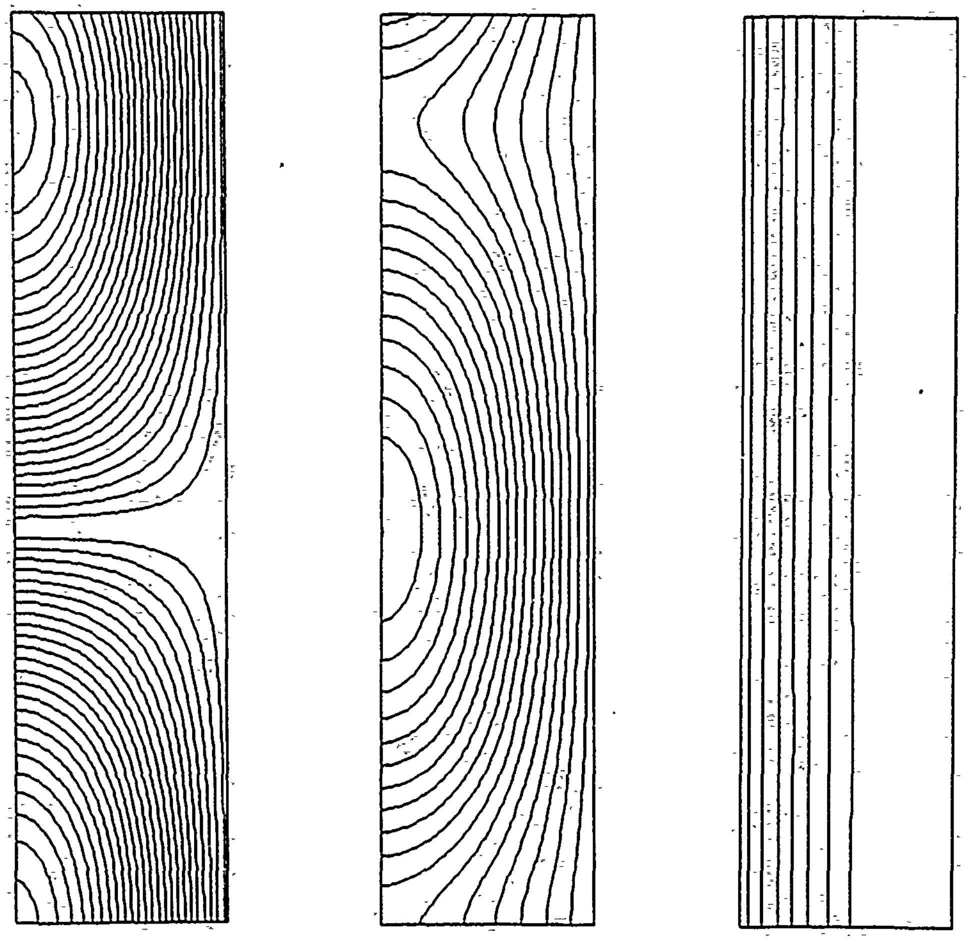

(b)

(a)

(c)

$\Delta E_x = 3000$ V/m

Figure 3. Undistorted axial electric field in a waveguide. (a) waveguide with reflecting end wall, (b) transmitting waveguide with one-dimensional method of characteristics, and (c) transmitting waveguide with proper characteristic boundary condition.

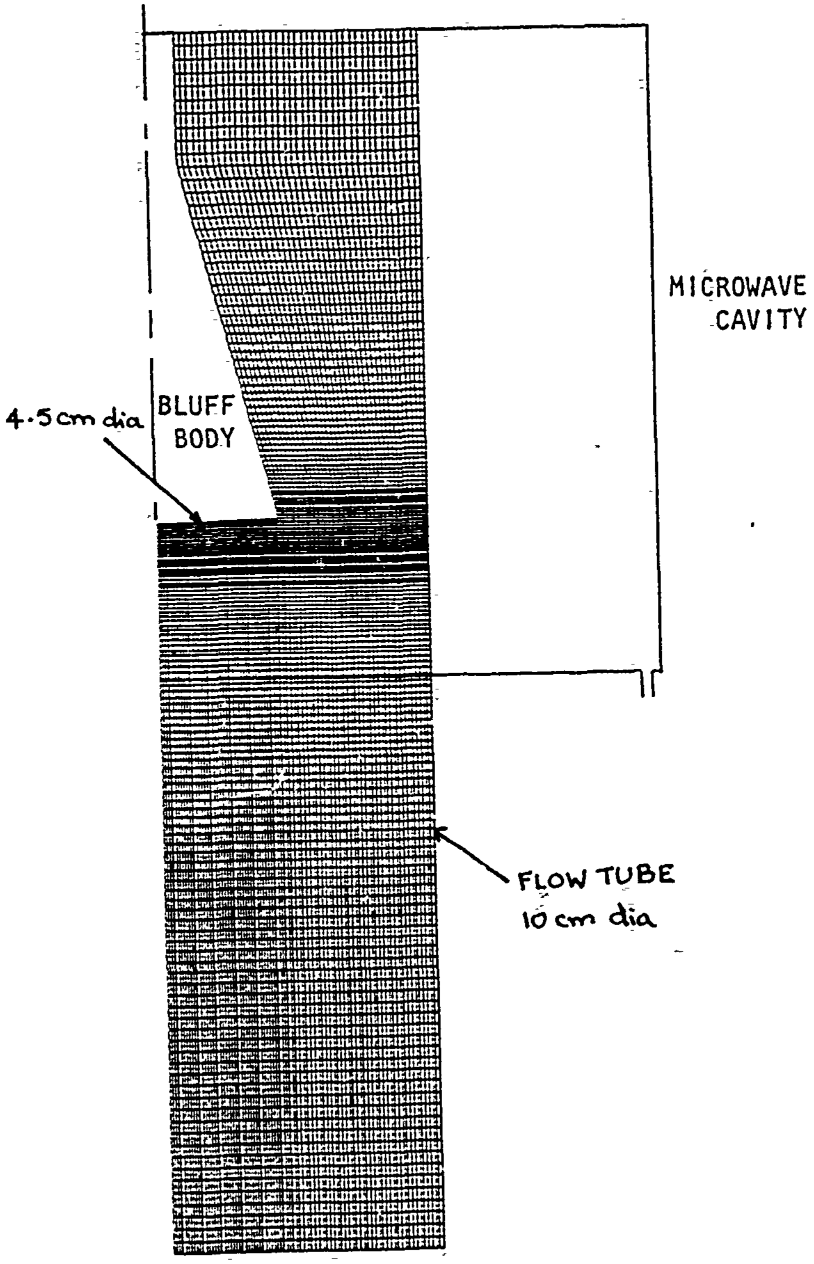

Figure 4. Fluid dynamic grid for axisymmetric bluff body geometry. Flow is from top to bottom.

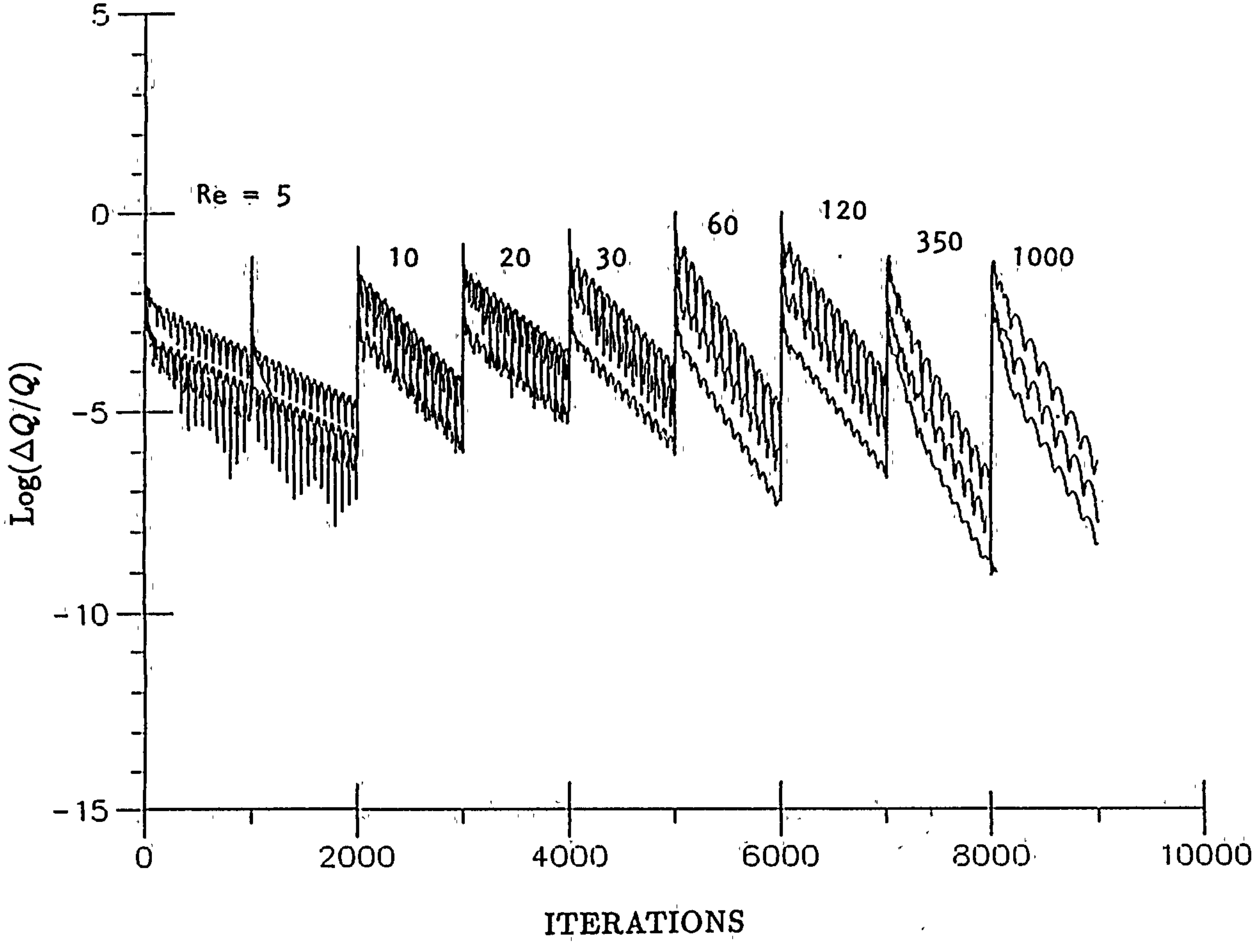

Figure 5. Convergence of low Mach number computations for the bluff body geometry at different Reynolds numbers.

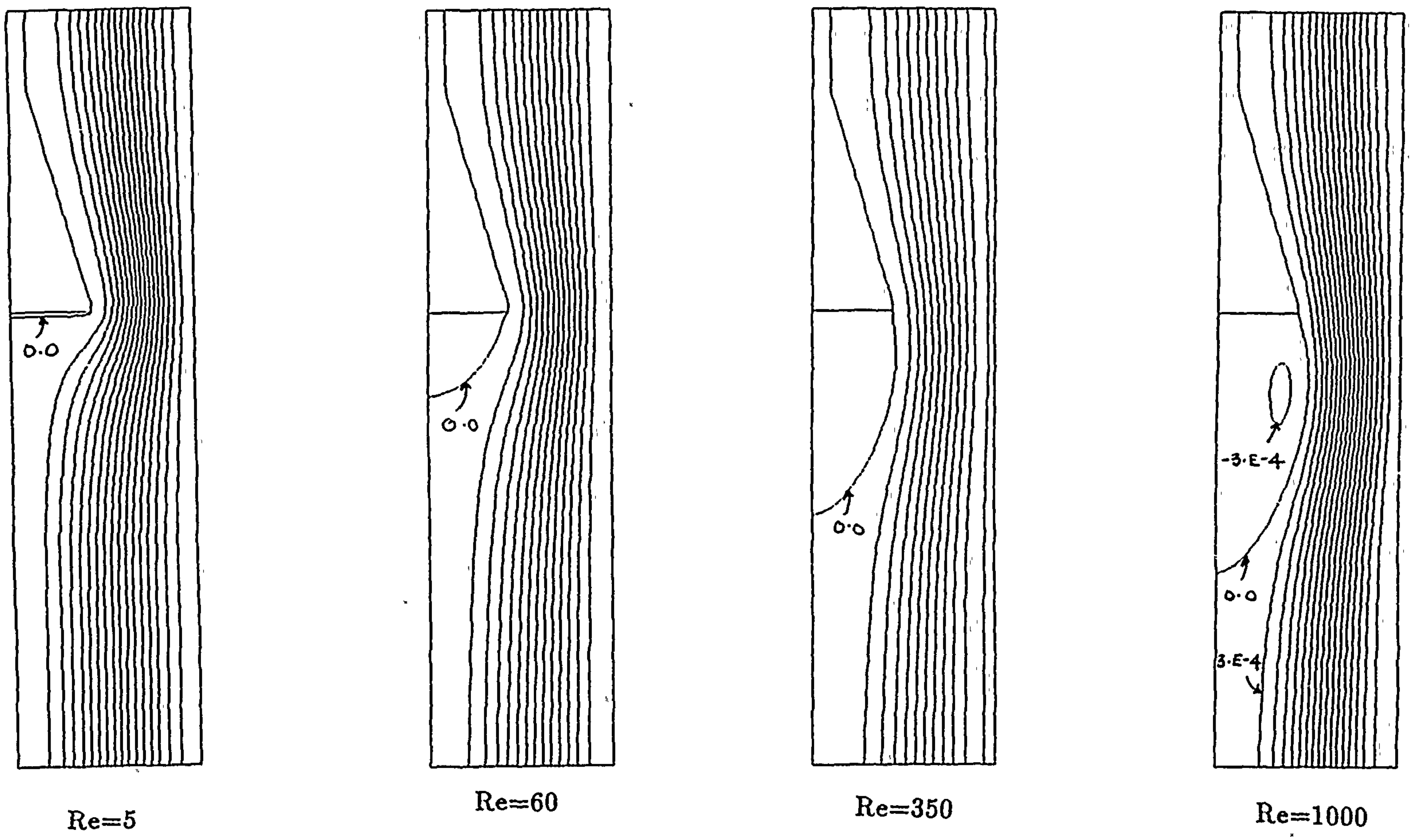

Re=5 Re=60 Re=350 Re=1000

Figure 6. Bluff body computations for different Reynolds numbers.
Re = 5, 60, 350, 1000.

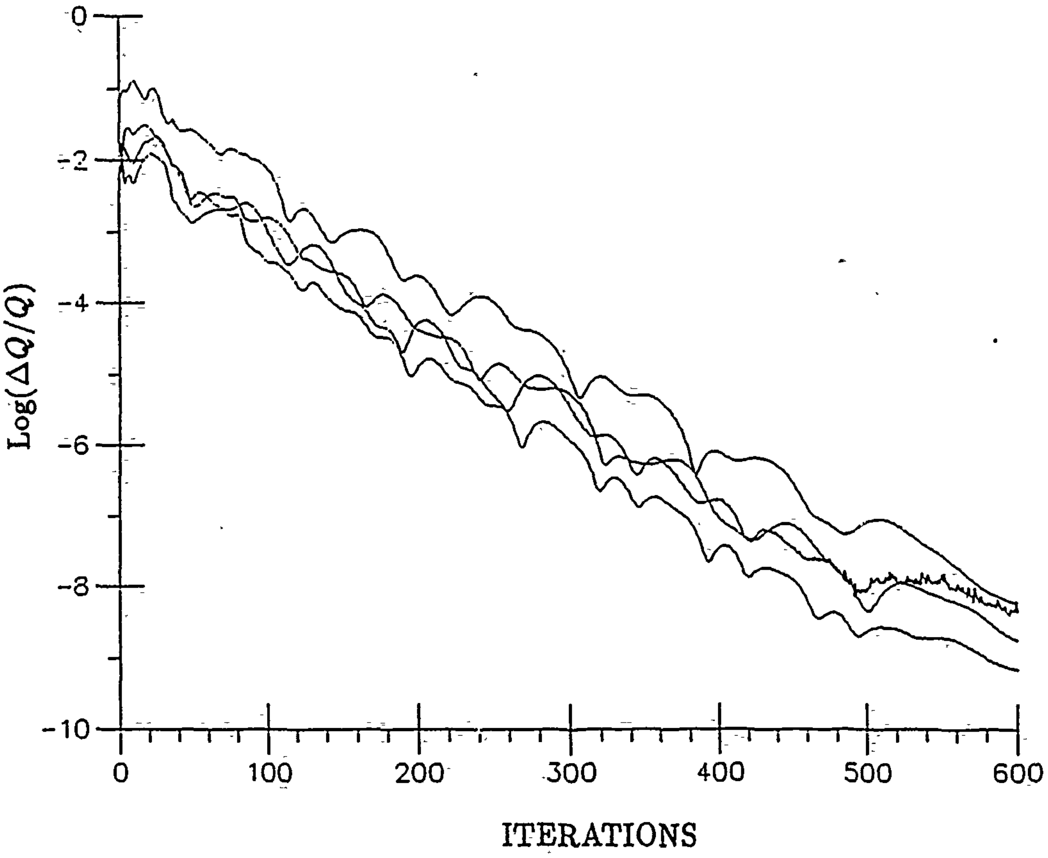

Figure 7. Convergence of coupled Navier-Stokes and Maxwell equations for the bluff body geometry using the TM_{011} mode.

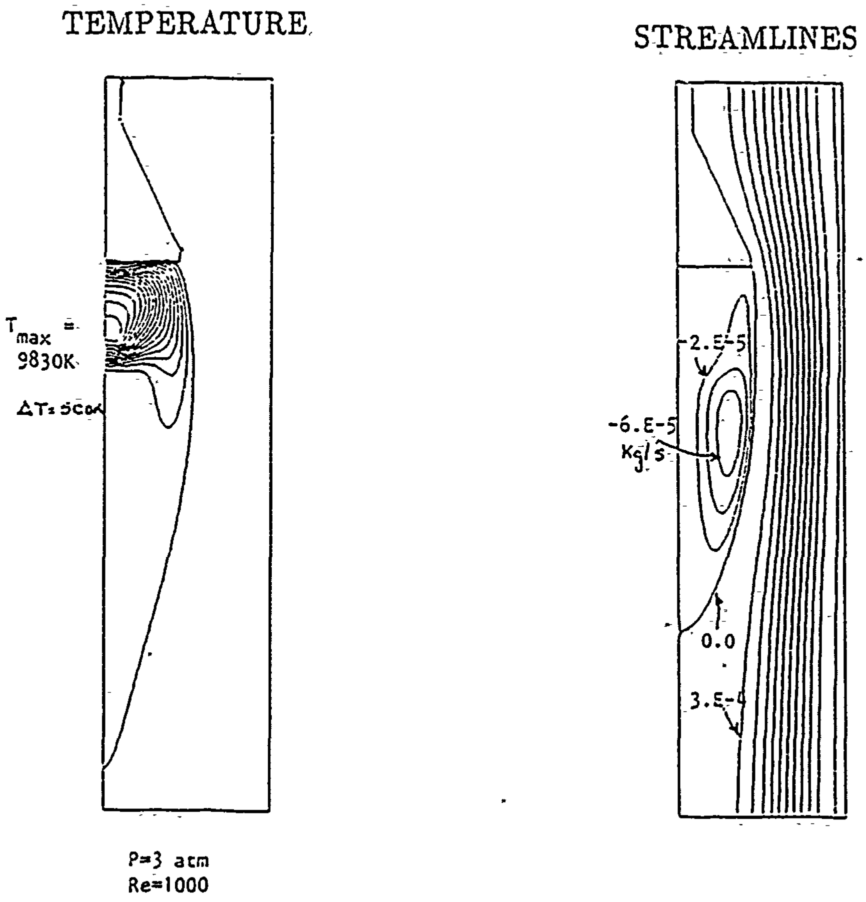

Figure 8. Representative flowfield for the bluff-body geometry. P_0 = 3 atm, P = 3 kW, Re = 1000.

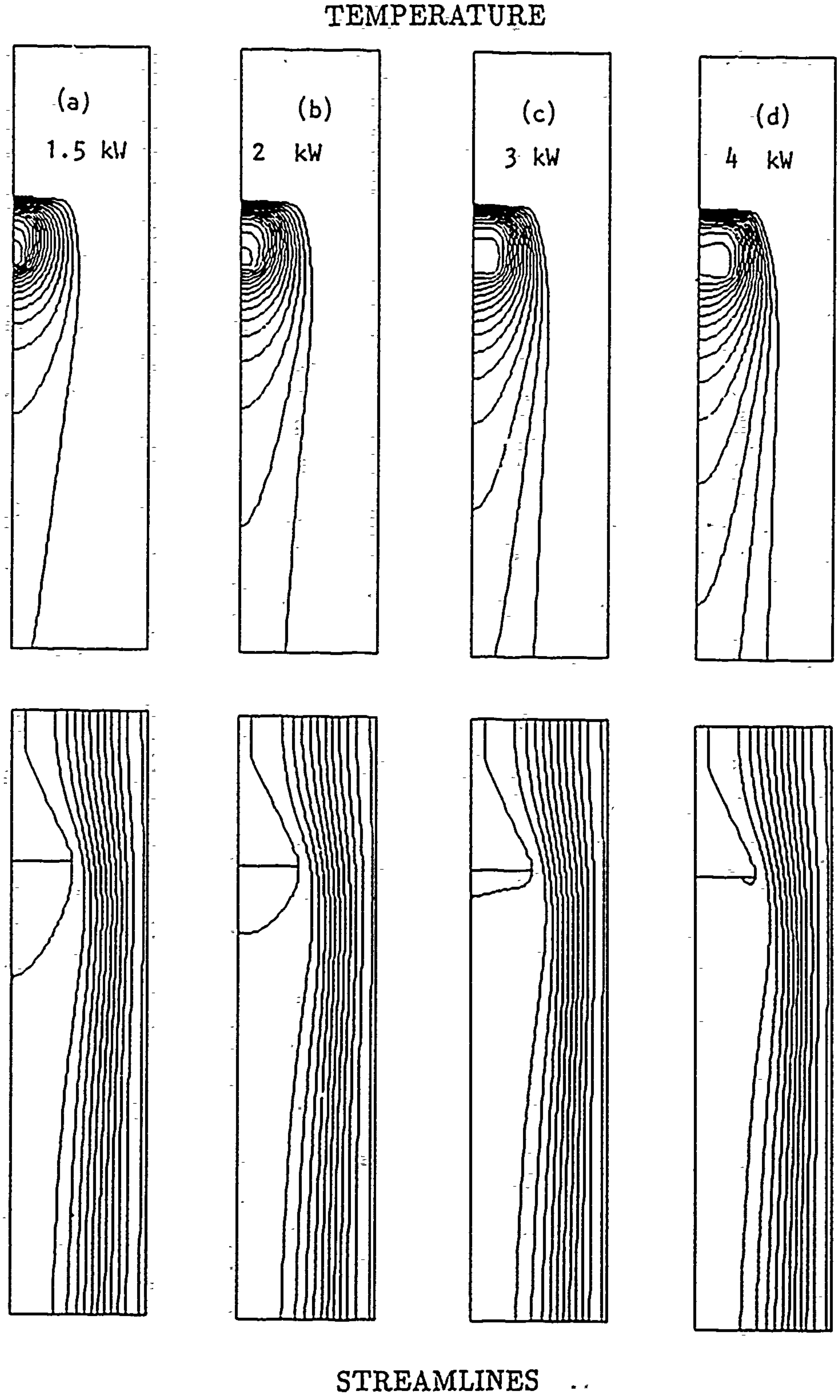

Figure 9. Effect of input power on bluff body plasmas.

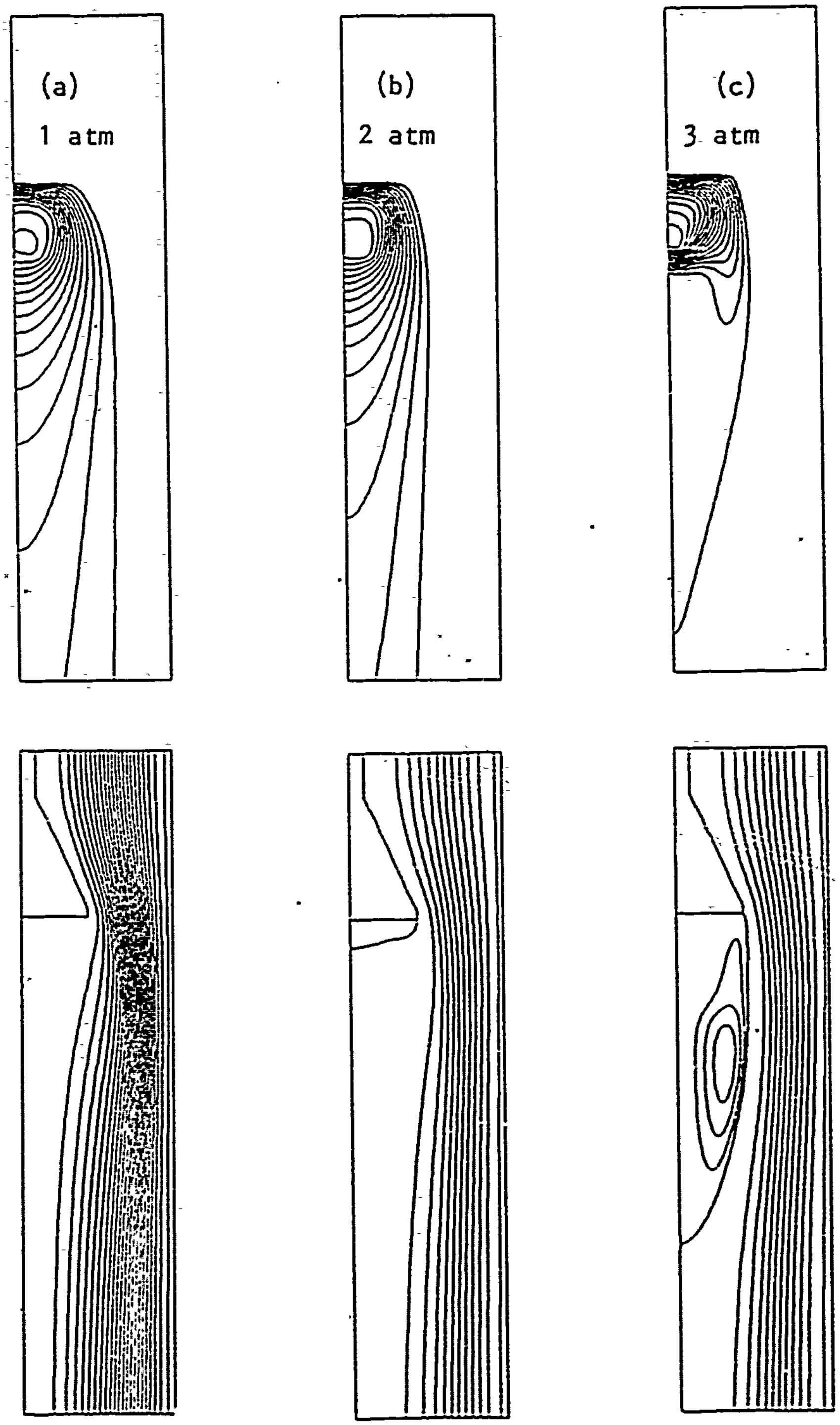

Figure 10. Effect of discharge pressure on bluff body plasmas.

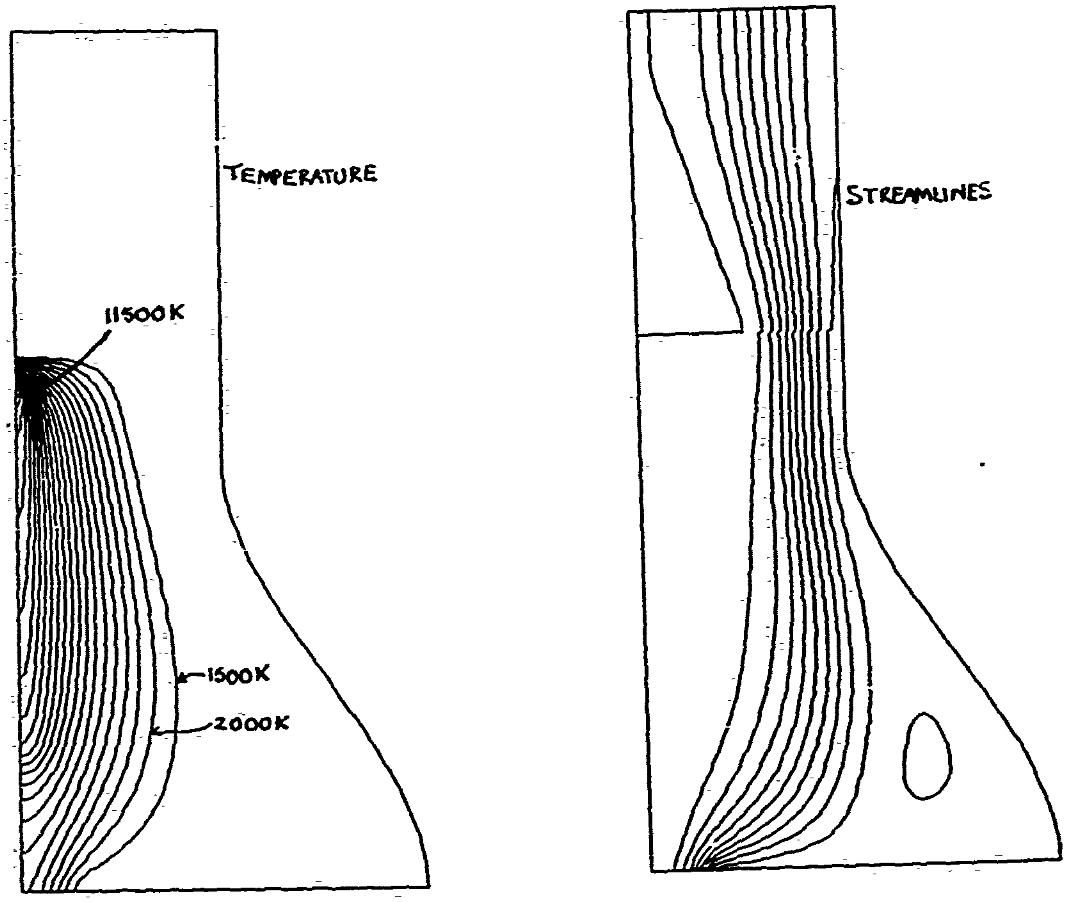

Figure 11. Representative solution for bluff-body stabilized resonant cavity plasma.

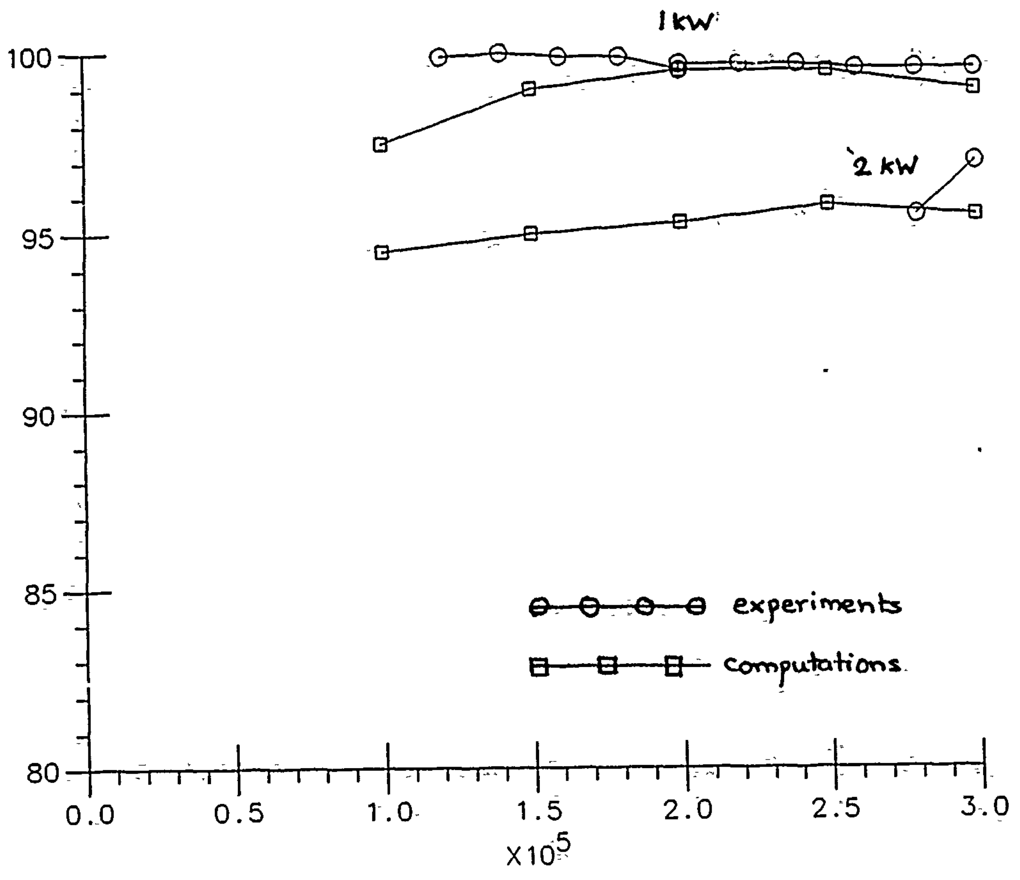

Figure 12. Coupling efficiency of bluff-body stabilized cavity plasmas. Comparison of predictions and experiments.

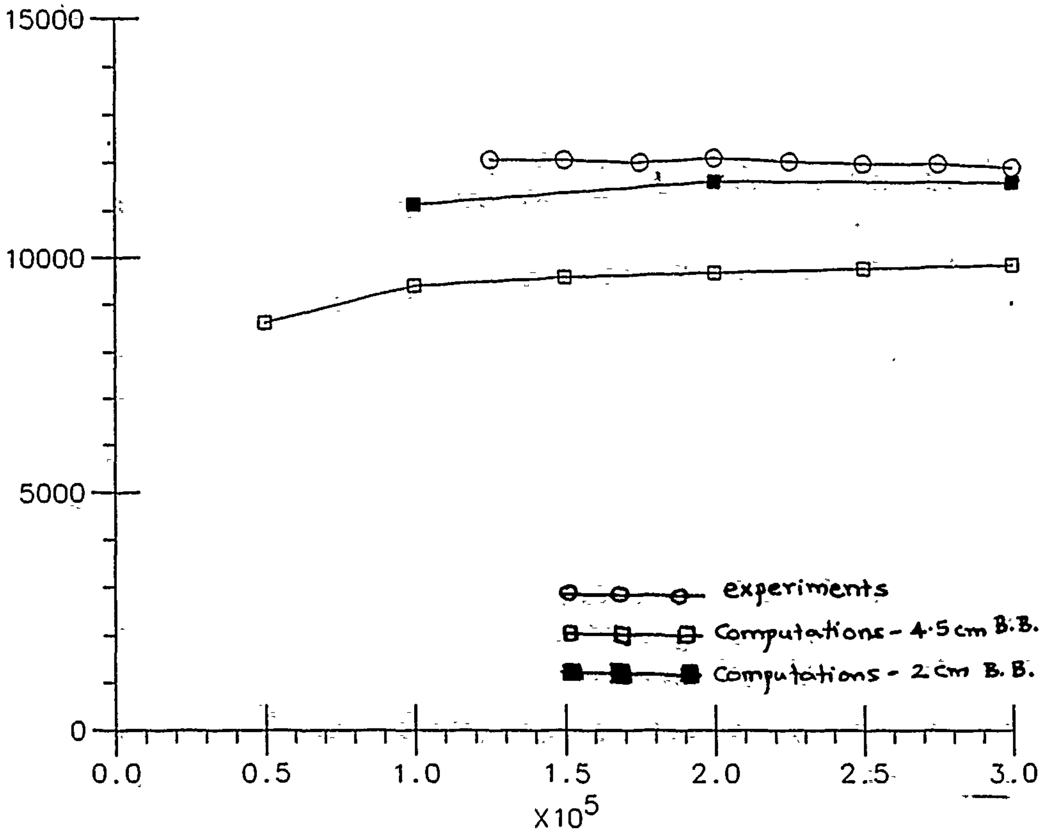

Figure 13. Peak temperature in bluff-body stabilized cavity plasmas. Comparison of predictions and experiments.

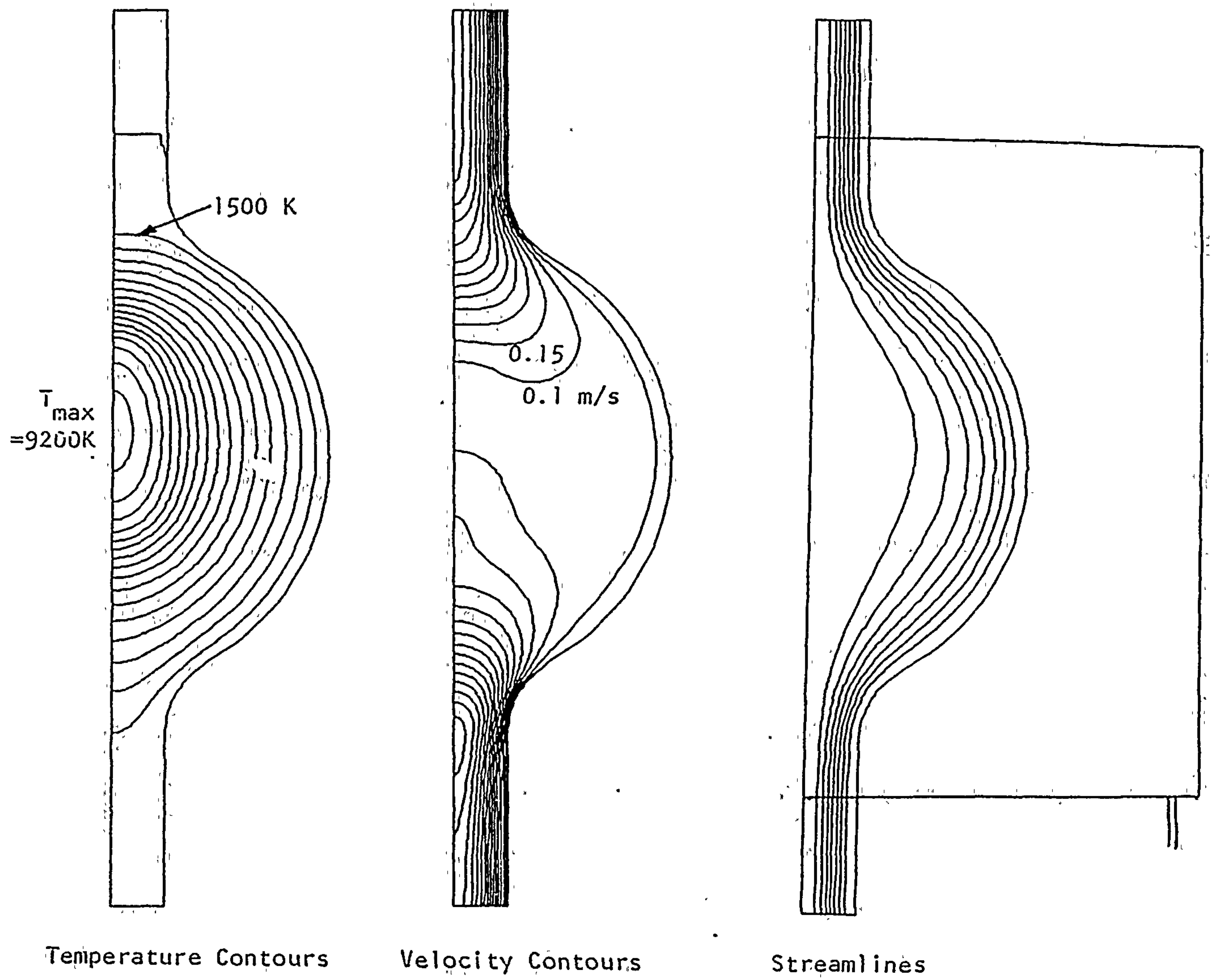

Temperature Contours Velocity Contours Streamlines

Figure 14. Representative solution of the sphere-cylinder configuration.
$P = 1$ atm, $\dot{m} = 1 \times 10^{-5}$ kg/s, Re=10, $P_{inc} = 3$ kW.

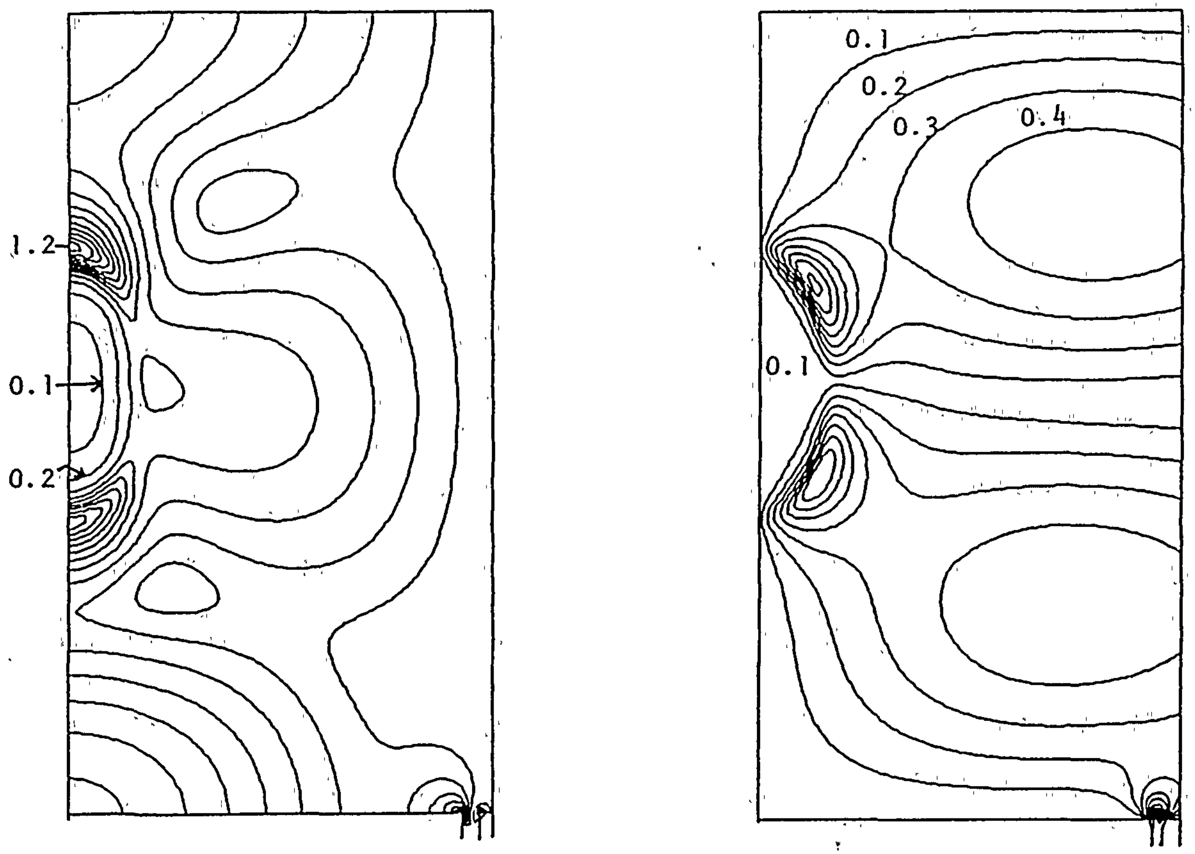

Axial Electric Field

Radial Electric Field

Figure 15. Distorted electric field solutions for the TM_{012} mode. The electric field lines are normalized by $E_{ref} = 25000$ V/m.

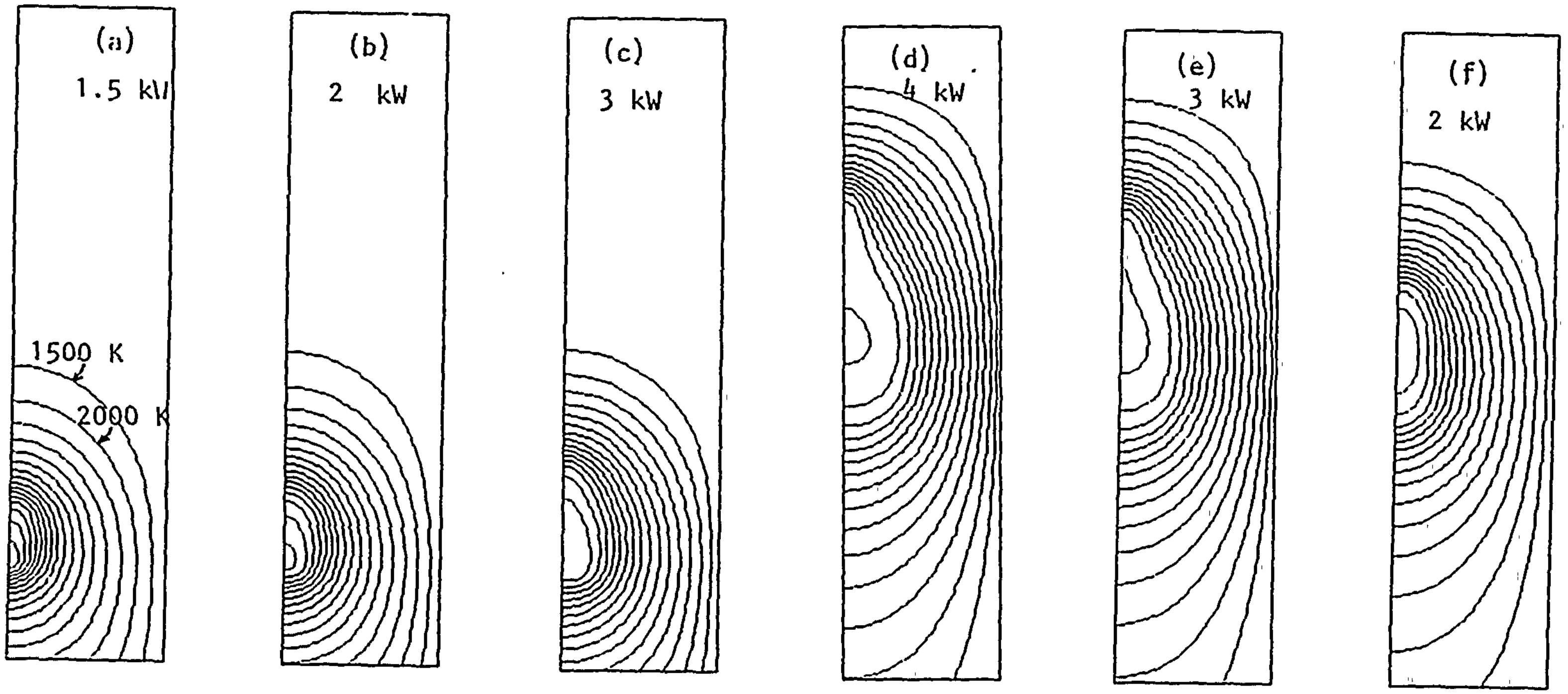

TEMPERATURE

Figure 16. Effect of input power on plasmas in a straight duct. $P_o = 1$ atm, $\dot{m} = 4.2 \times 10^{-5}$ kg/s.

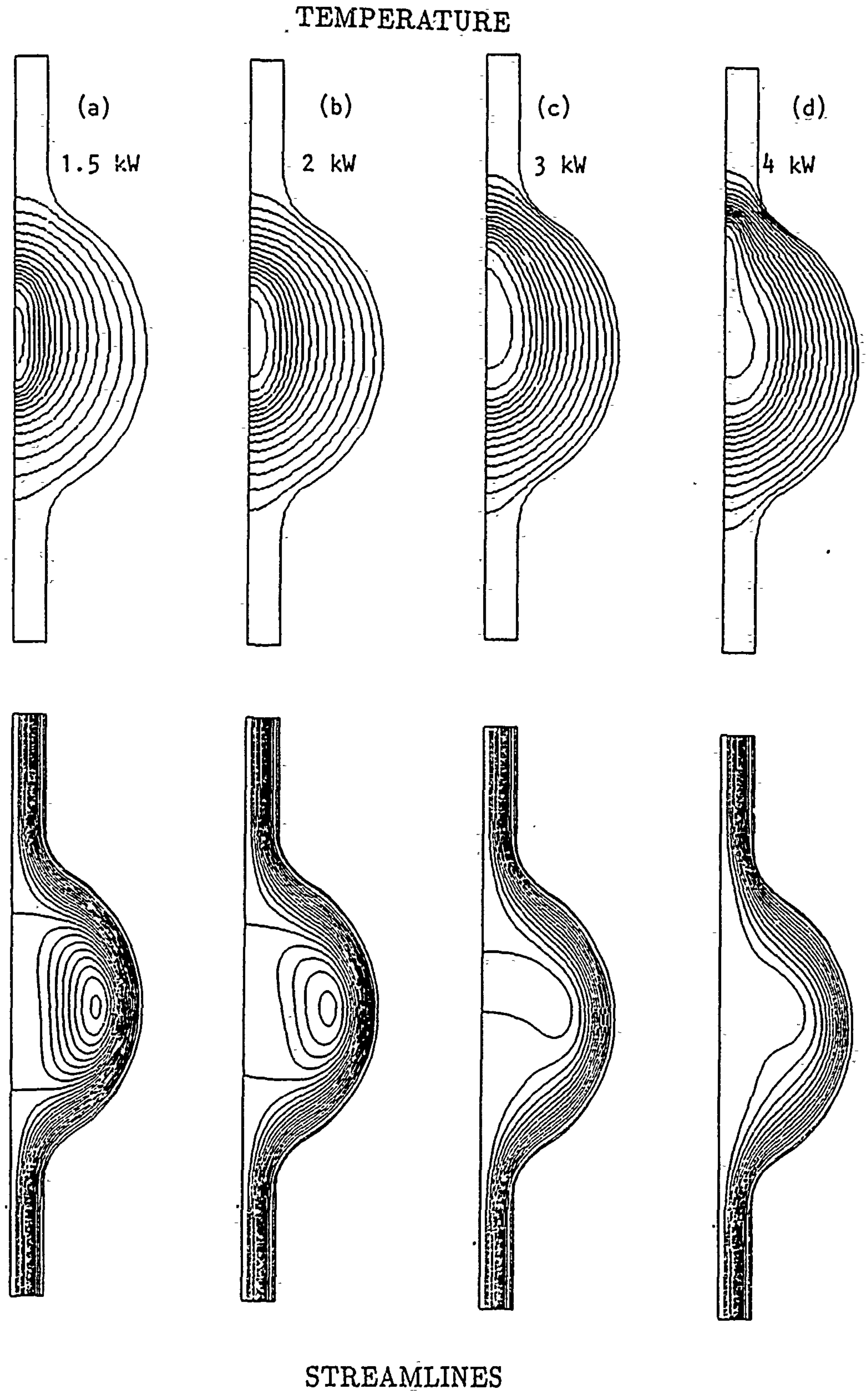

Figure 17. Effect of input power on plasmas in the sphere-cylindrial tube. $P_o = 1$ atm, $\dot{m} = 2.6 \times 10^{-6}$ kg/s.

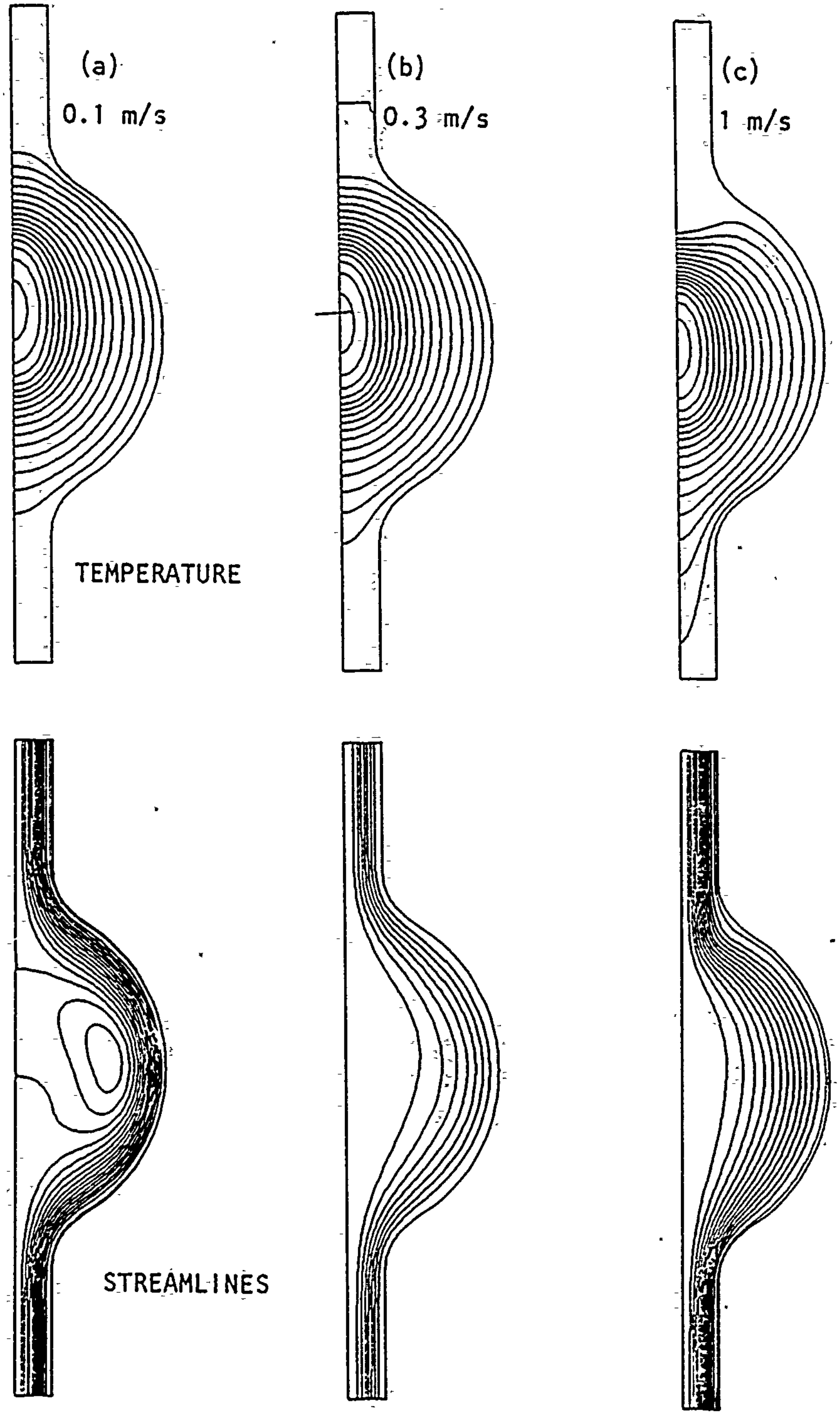

Figure 18. Effect of gas velocity on sphere-cylinder plasmas.
$P_o = 1$ atm, $P = 3$ kW.

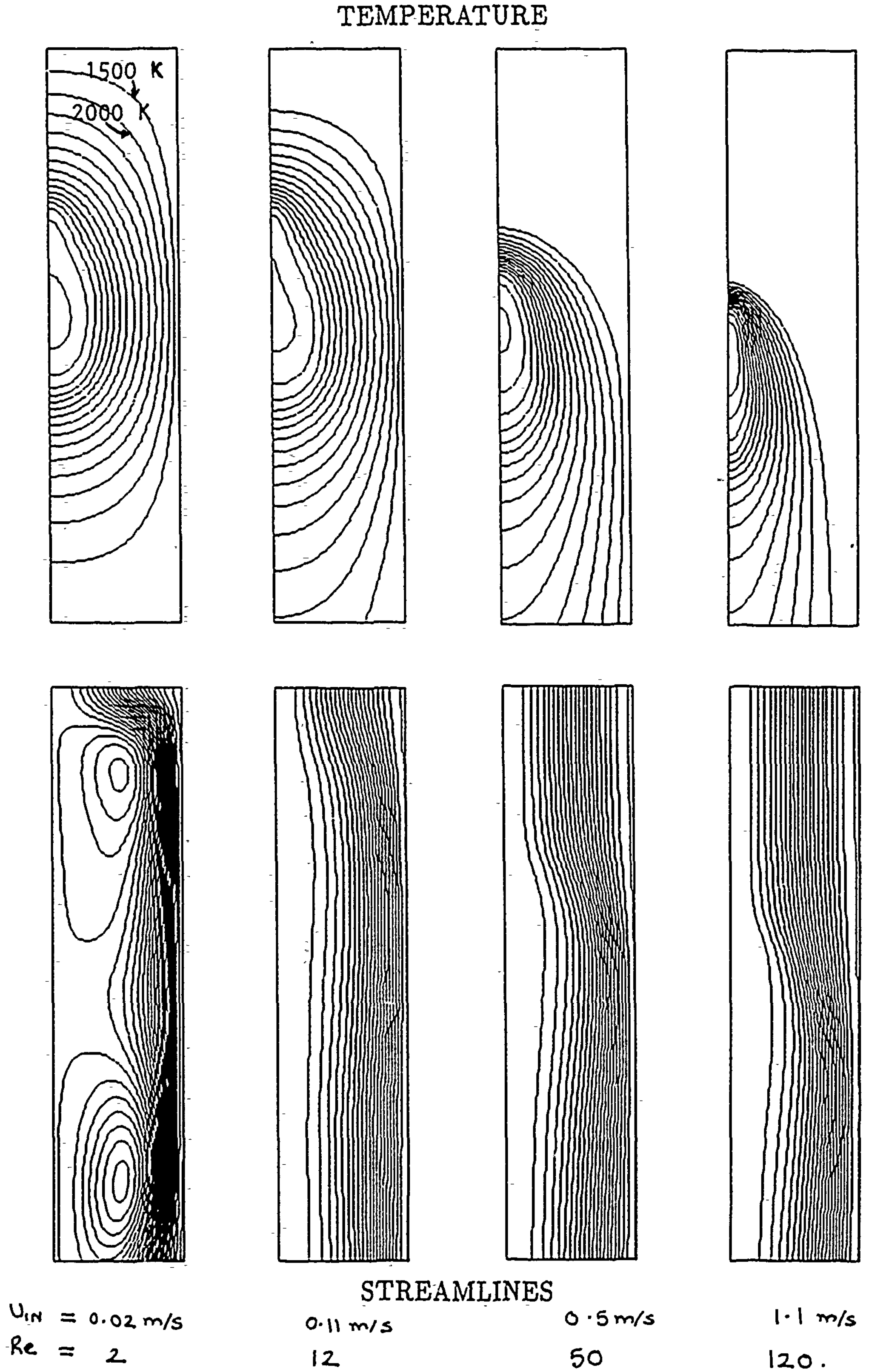

Figure 19. Effect of gas velocity variation on straight duct plasmas. $P_o = 1$ atm, $P = 3$ kW.

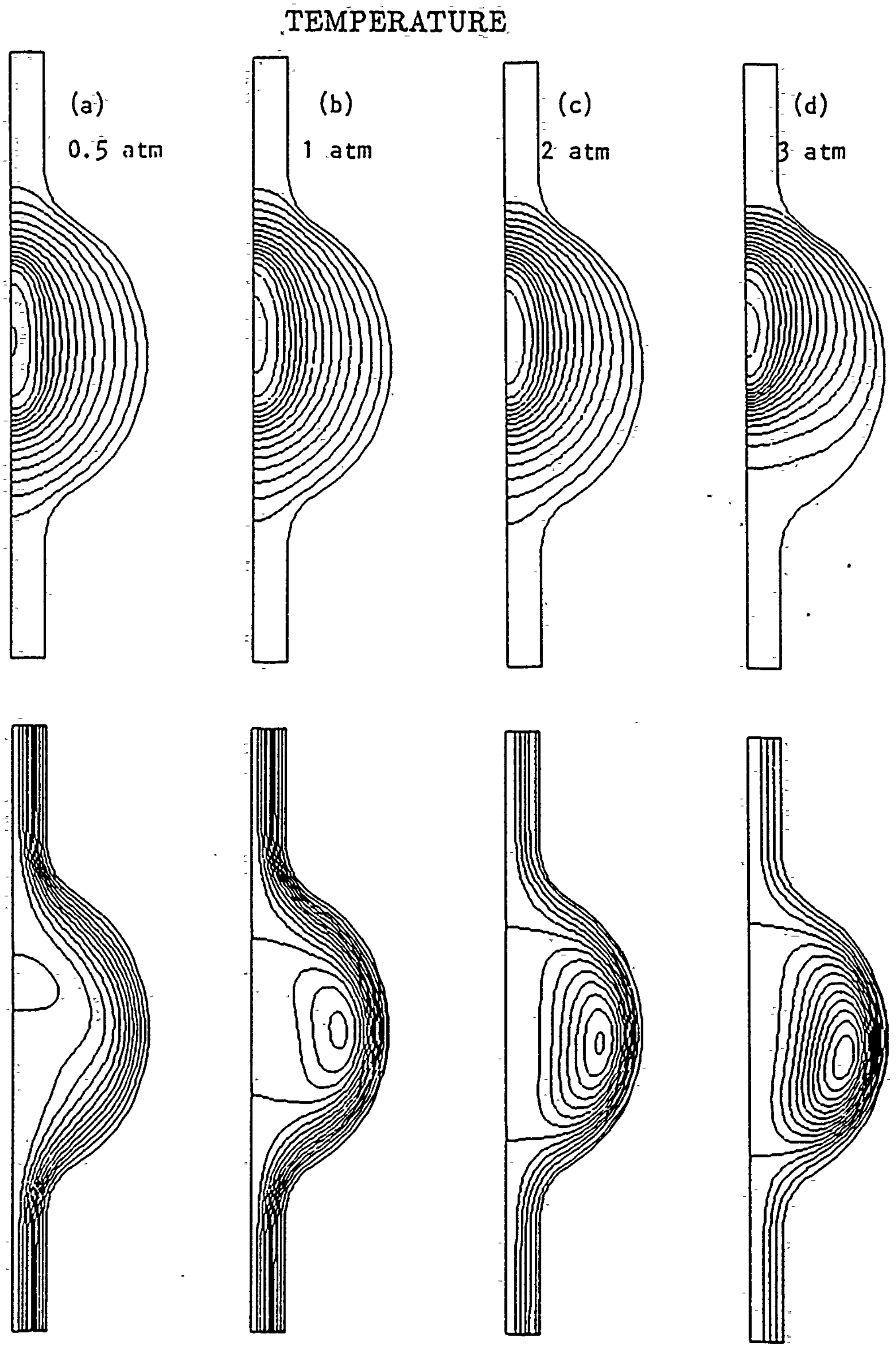

Figure 20. Effect of discharge pressure on sphere-cylinder plasmas.

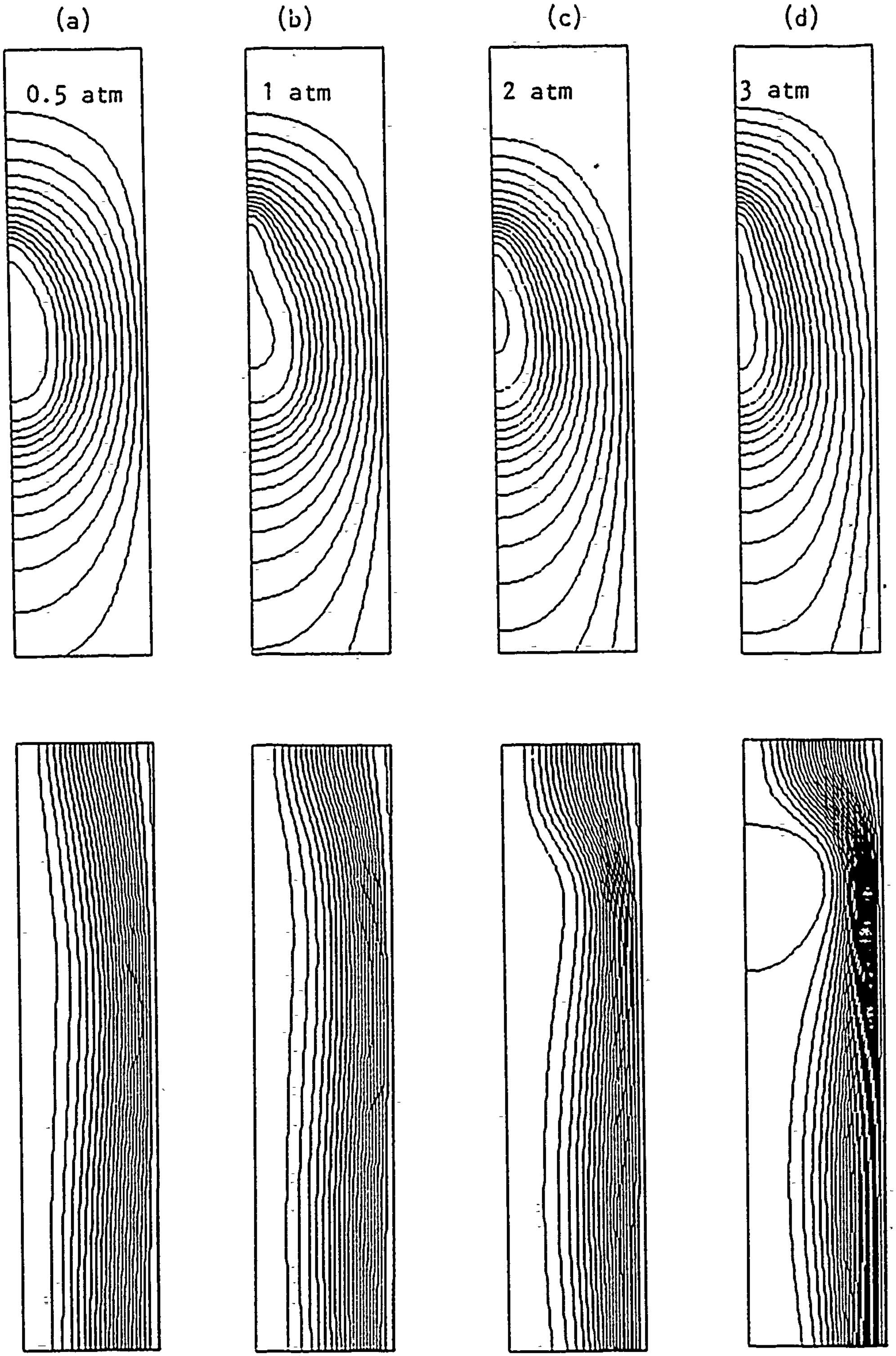

Figure 21. Effect of discharge pressure on straight duct plasmas. $P = 3$ kW.

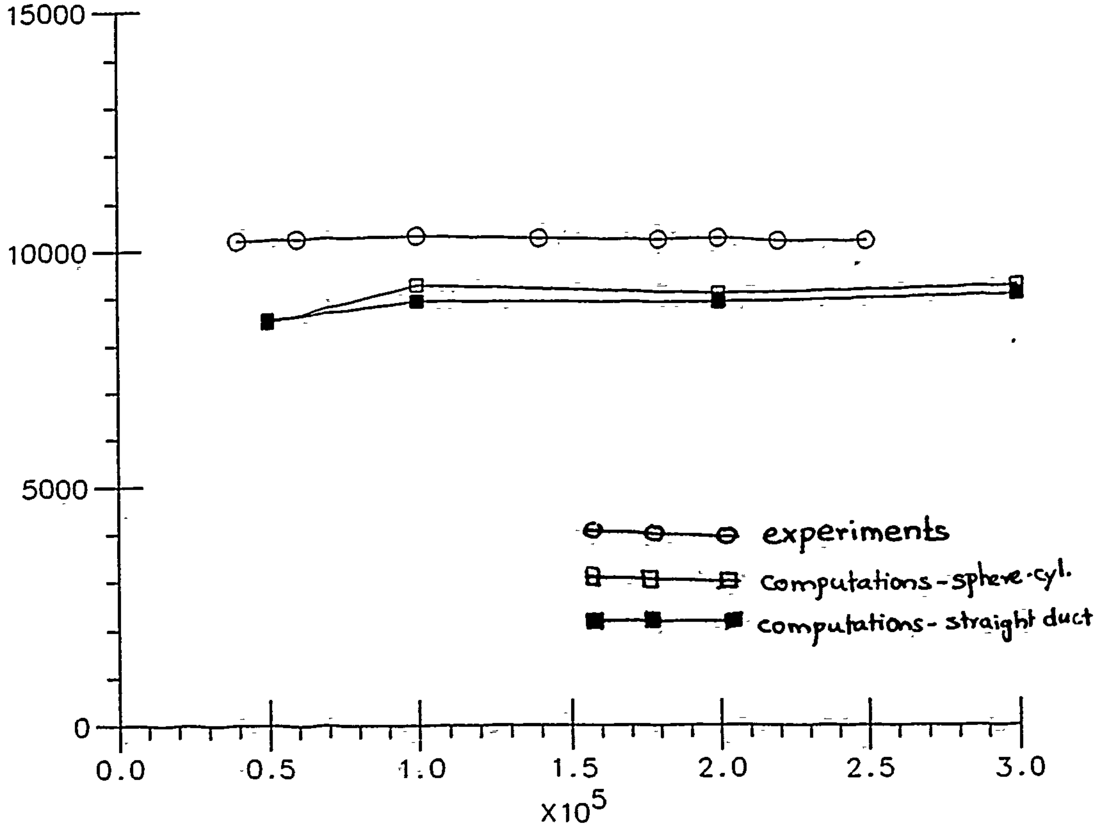

Figure 22. Peak temperature for free-floating cavity plasmas. Comparison of predictions and experiments.

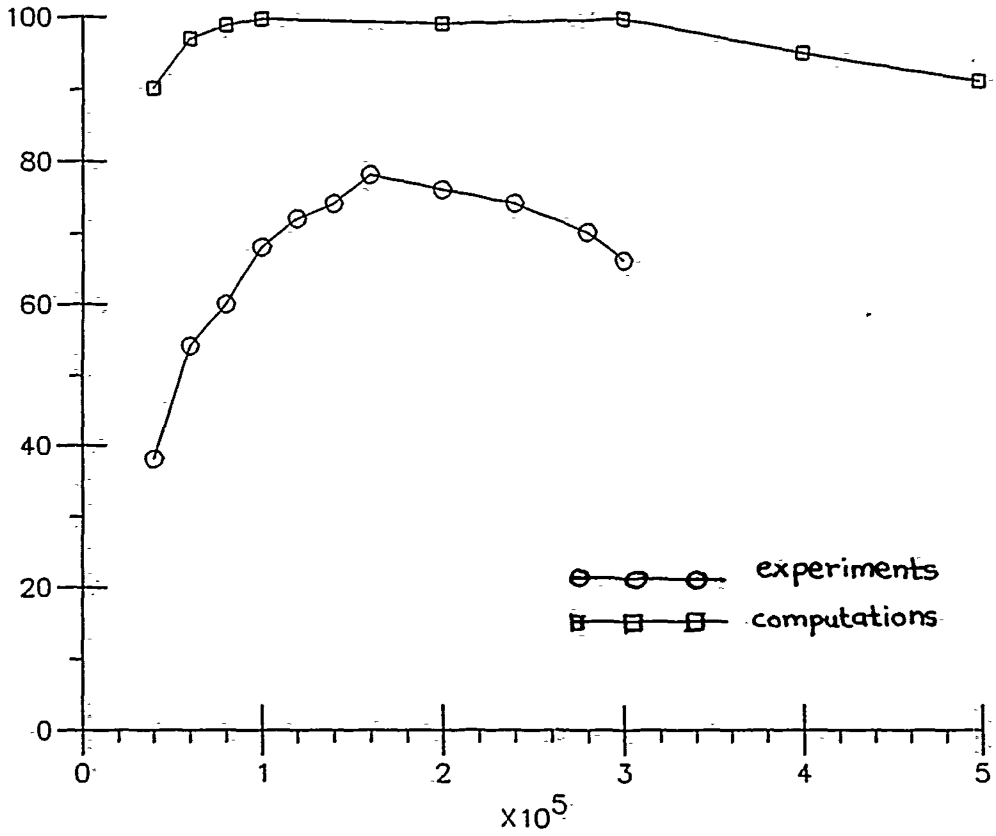

Figure 23. Coupling efficiency of free-floating cavity plasmas. Comparison of predictions and experiments.

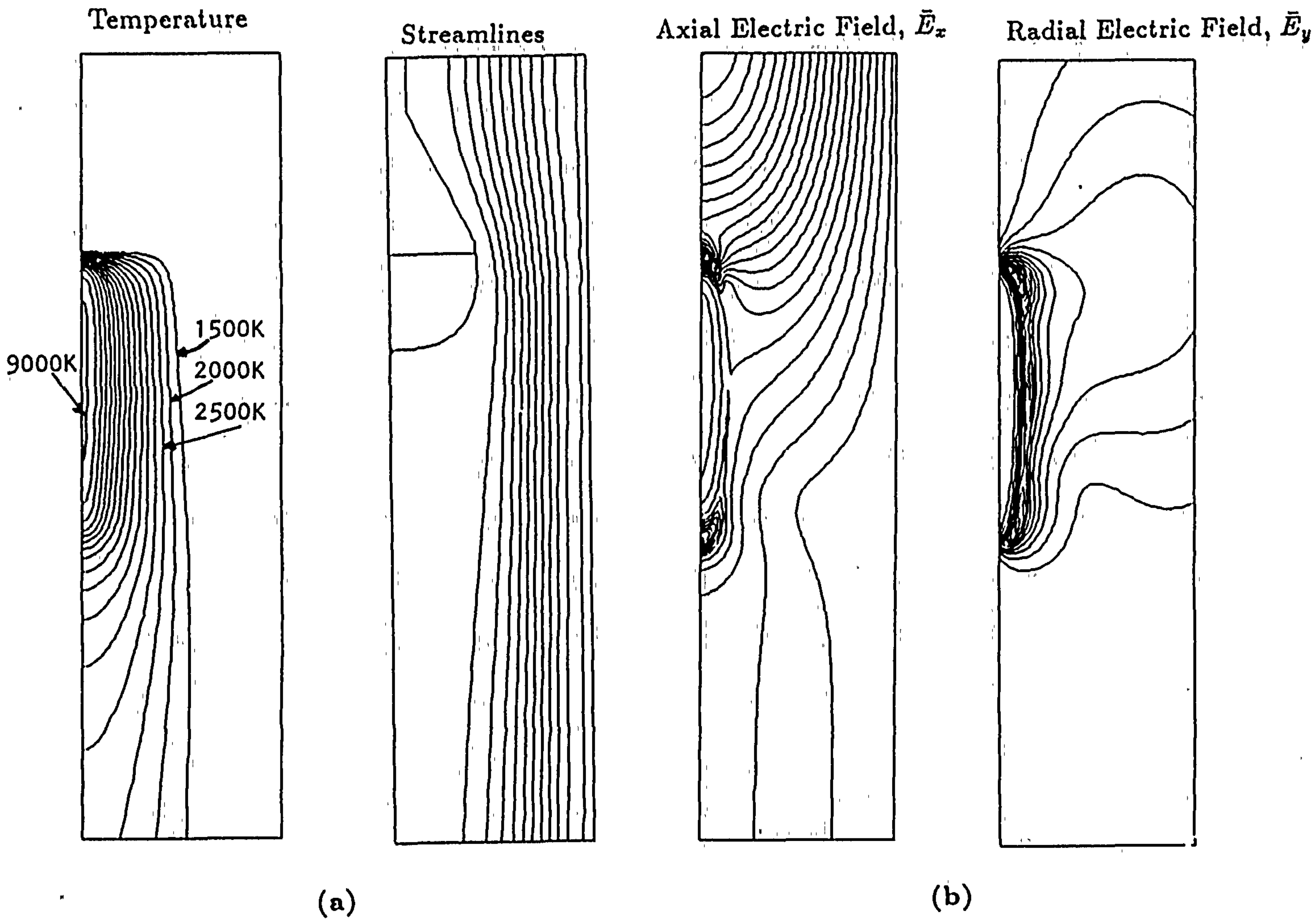

Figure 24. Solution field for plasma generated in a waveguide with a turbulent boundary. Power 3.5 kW, pressure 1 atm, gas velocity 3 m/s, mass flow 1.1 g/s, D_b = 4.5 cm. (a) Flowfield solution showing temperature and streamline contours, and (b) Electric field lines.

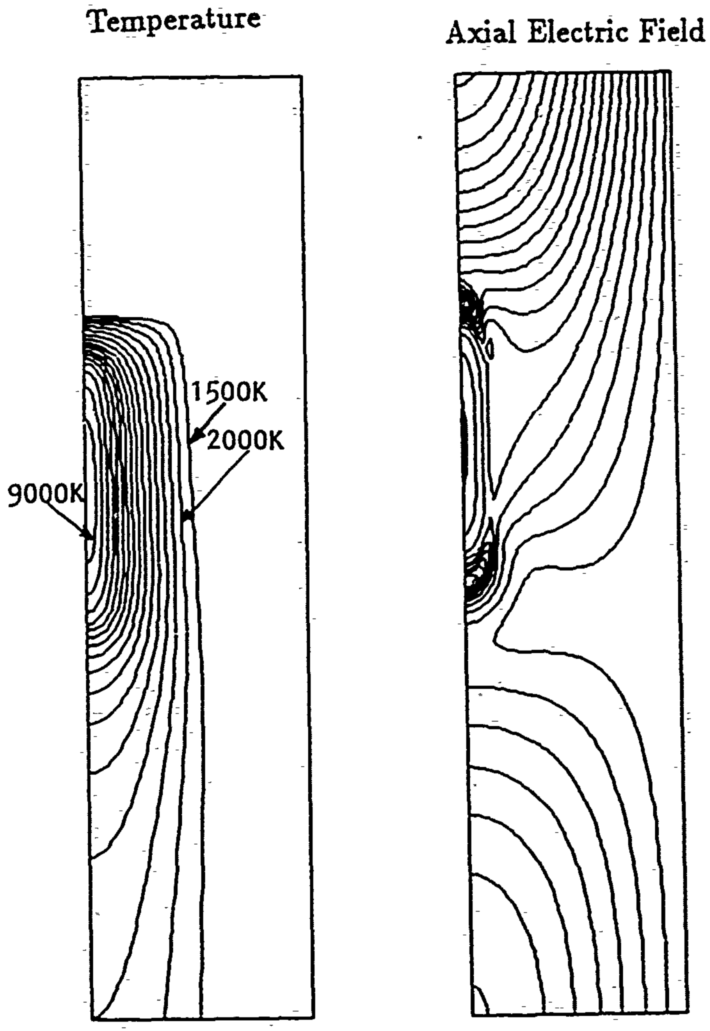

Temperature

Axial Electric Field

Figure 25. Temperature contours and axial electric field for reflecting waveguide configuration.

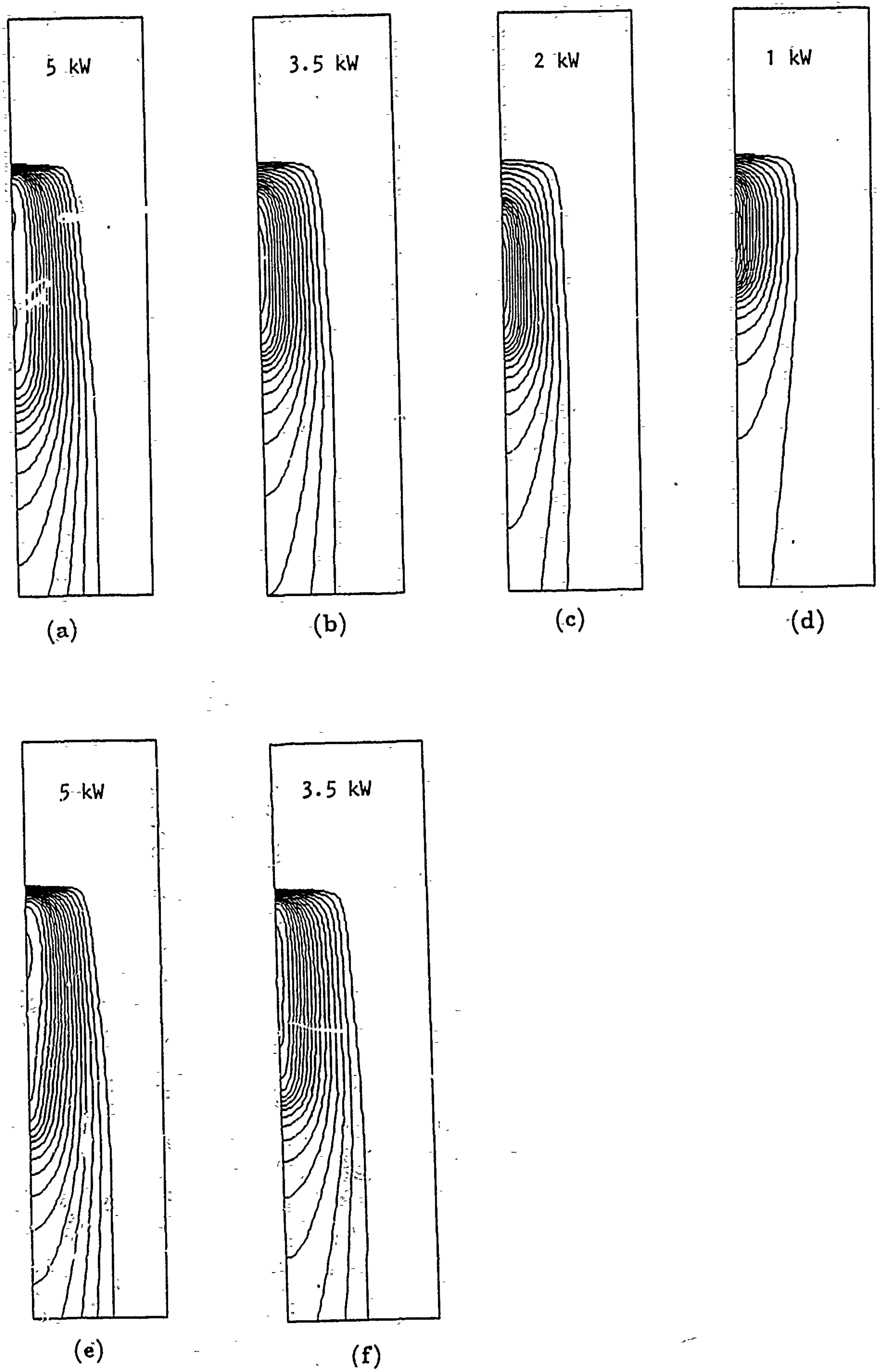

Figure 26. Effect of power variation on (a)-(d) reflecting, and (e)-(f) transmitting configurations.

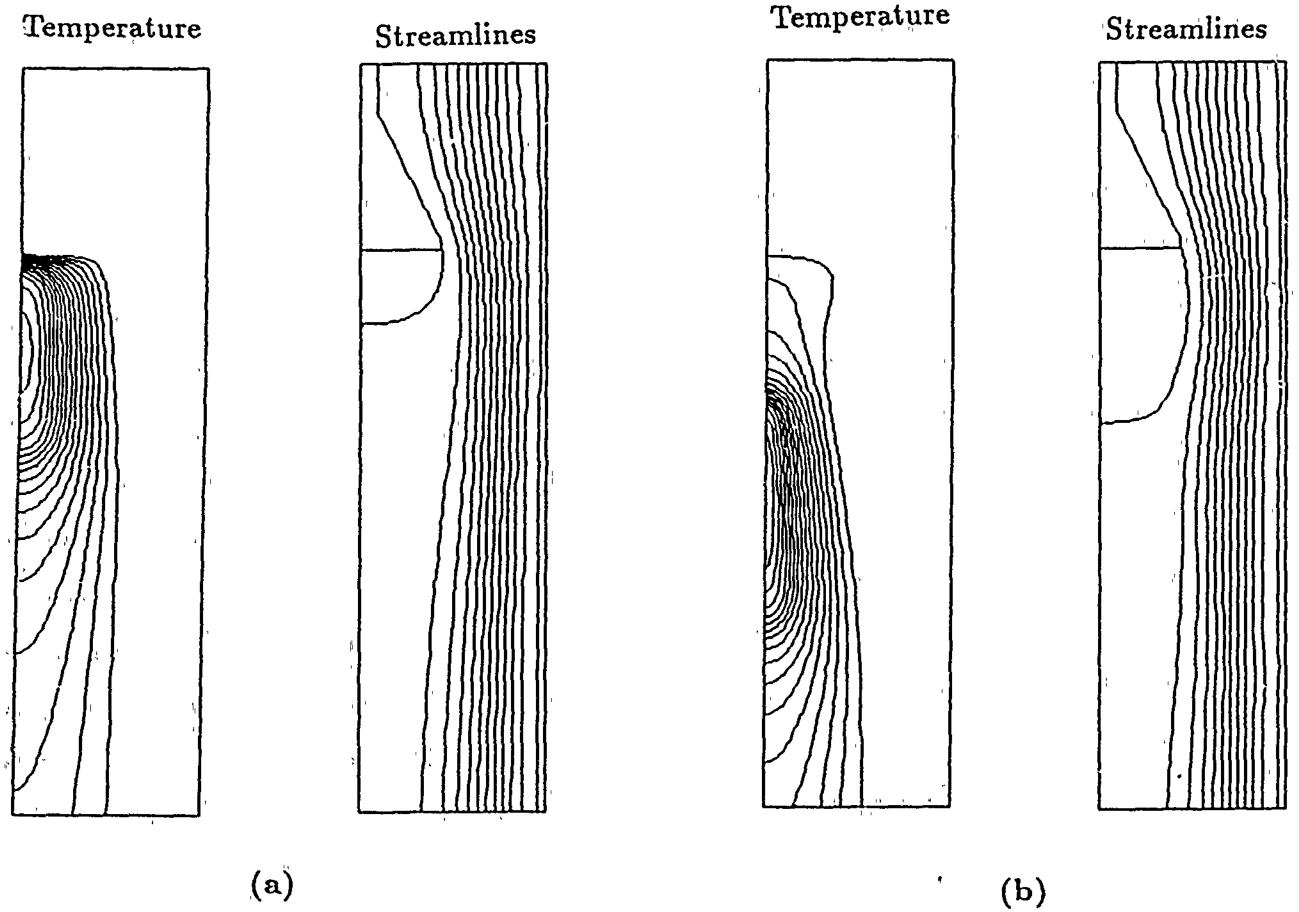

Figure 27. Variation in plasma location when the reflecting end wall is moved further downstream.

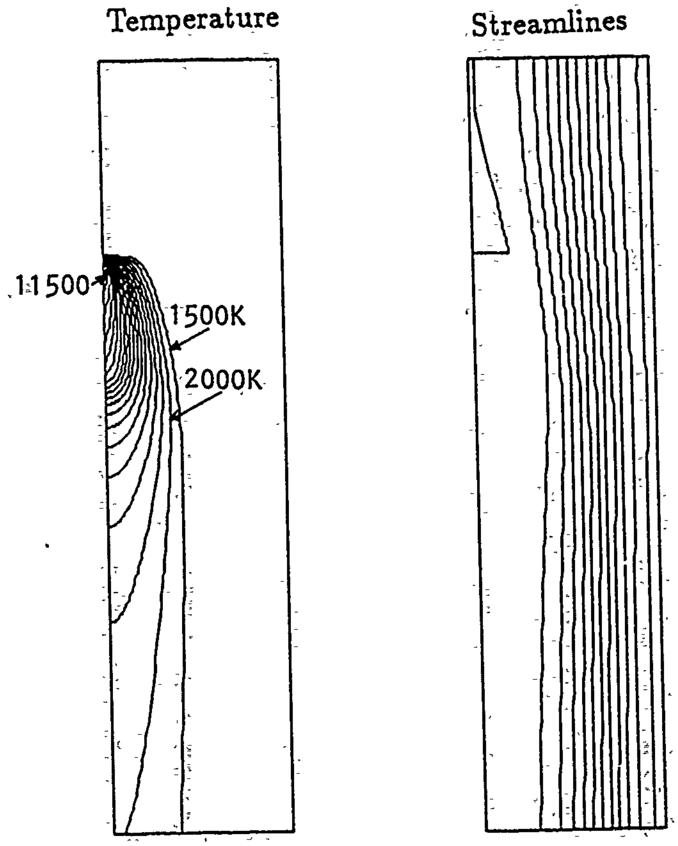

Figure 28. Temperature and streamline contours for smaller bluff body; $D_b = 2$ cm. P=3 kW.

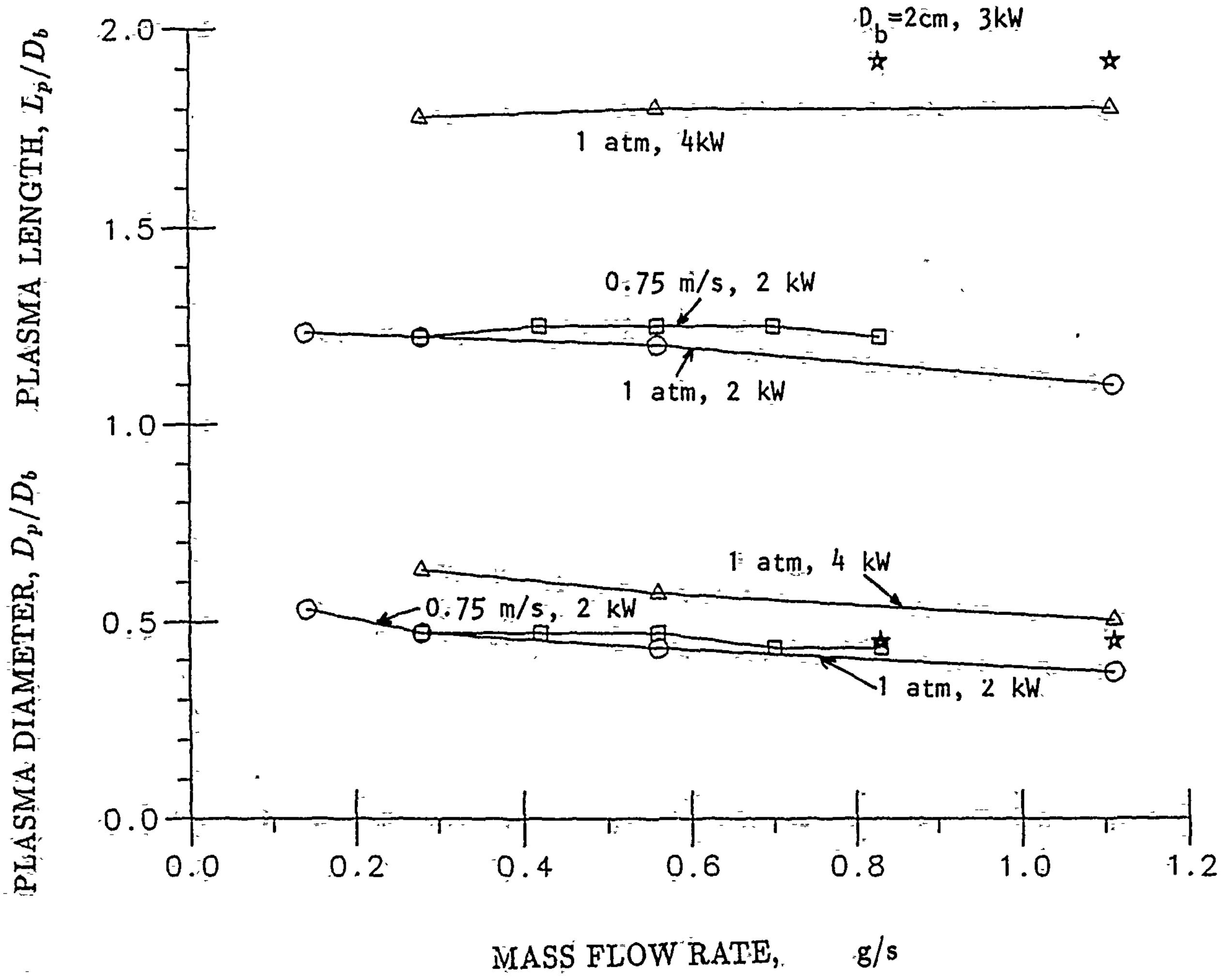

Figure 29. Variation in plasma length and mean diameter as a function of mass flow rate.

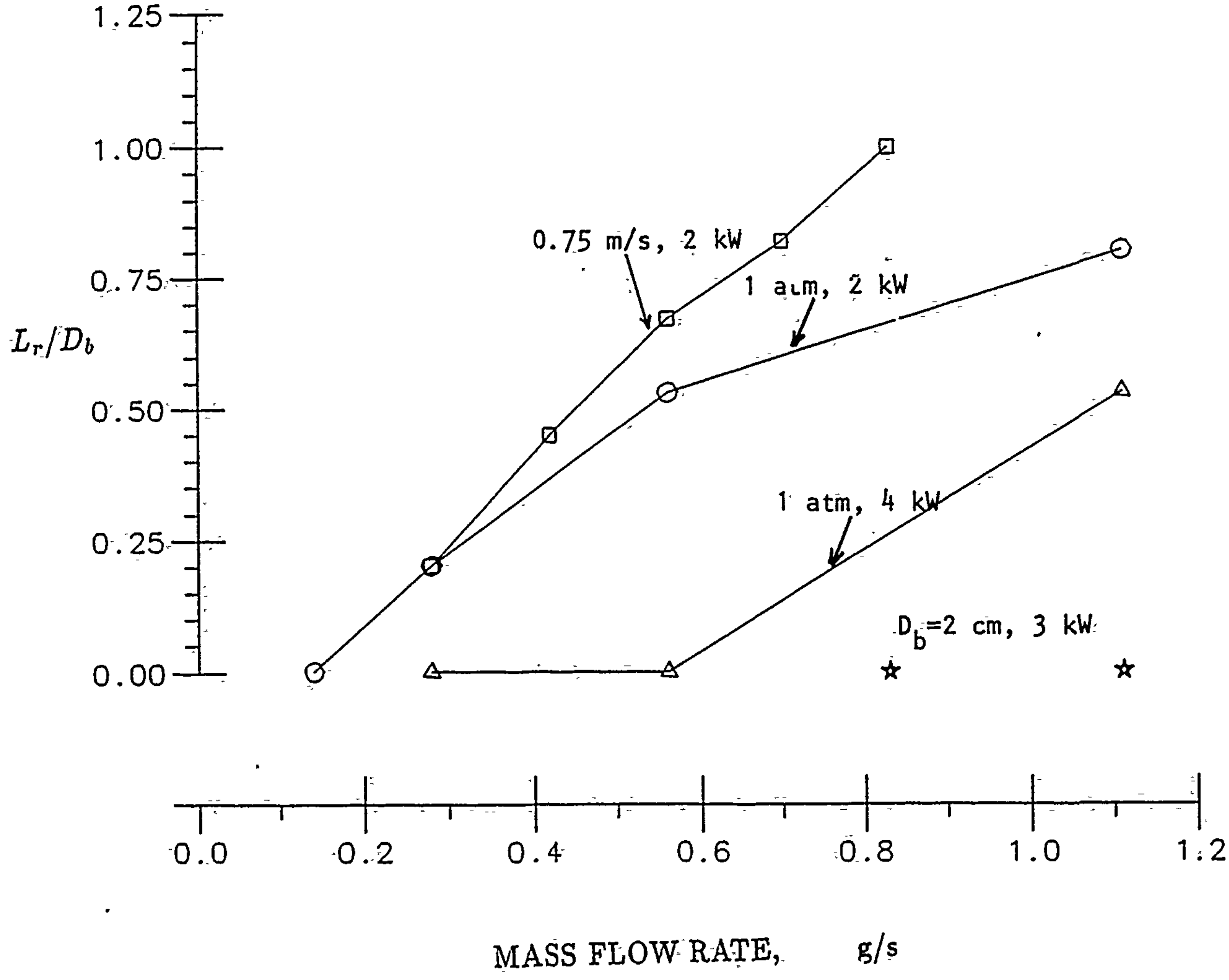

Figure 30. Variation in length of recirculation zone as a function of mass flow rate.

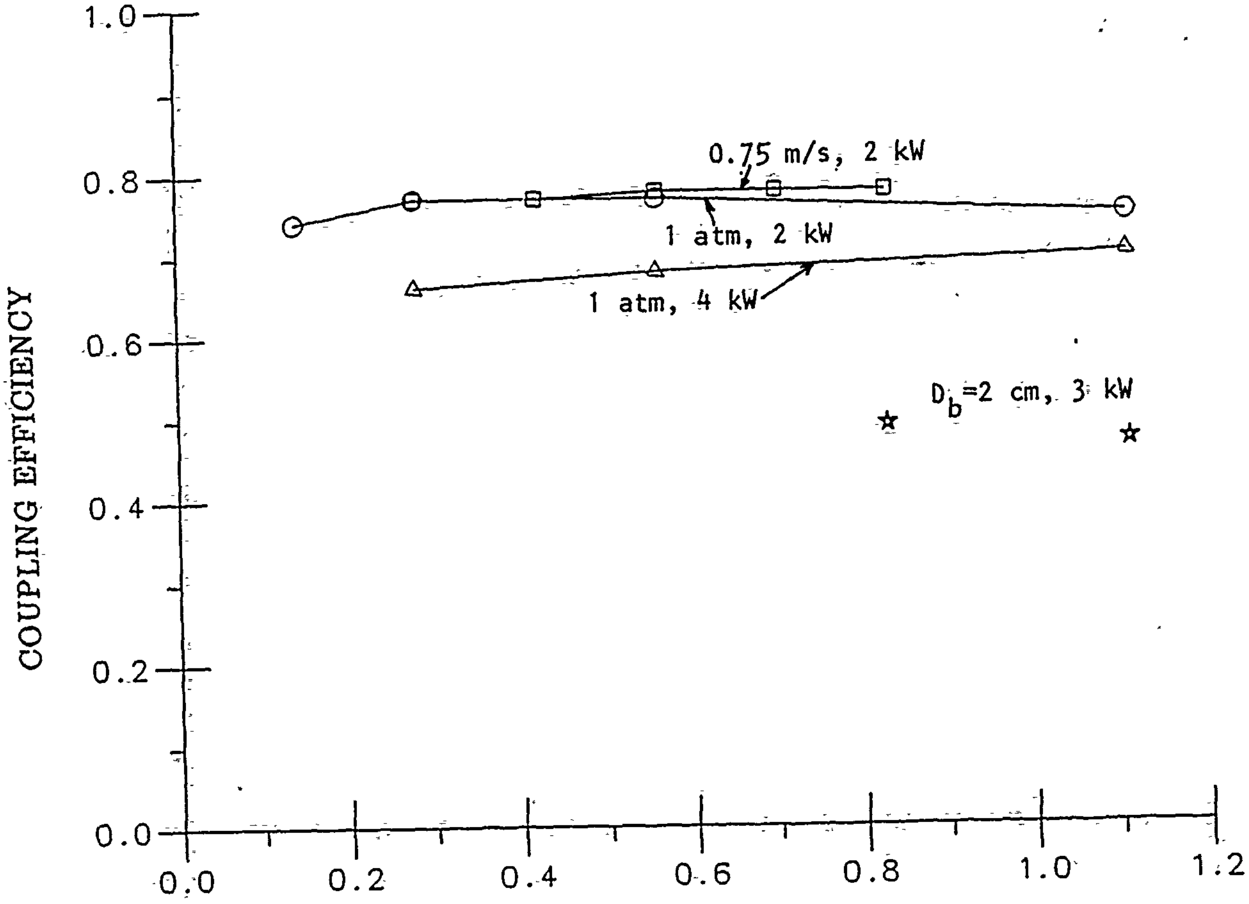

Figure 31. Coupling efficiency as a function of mass flow rate.

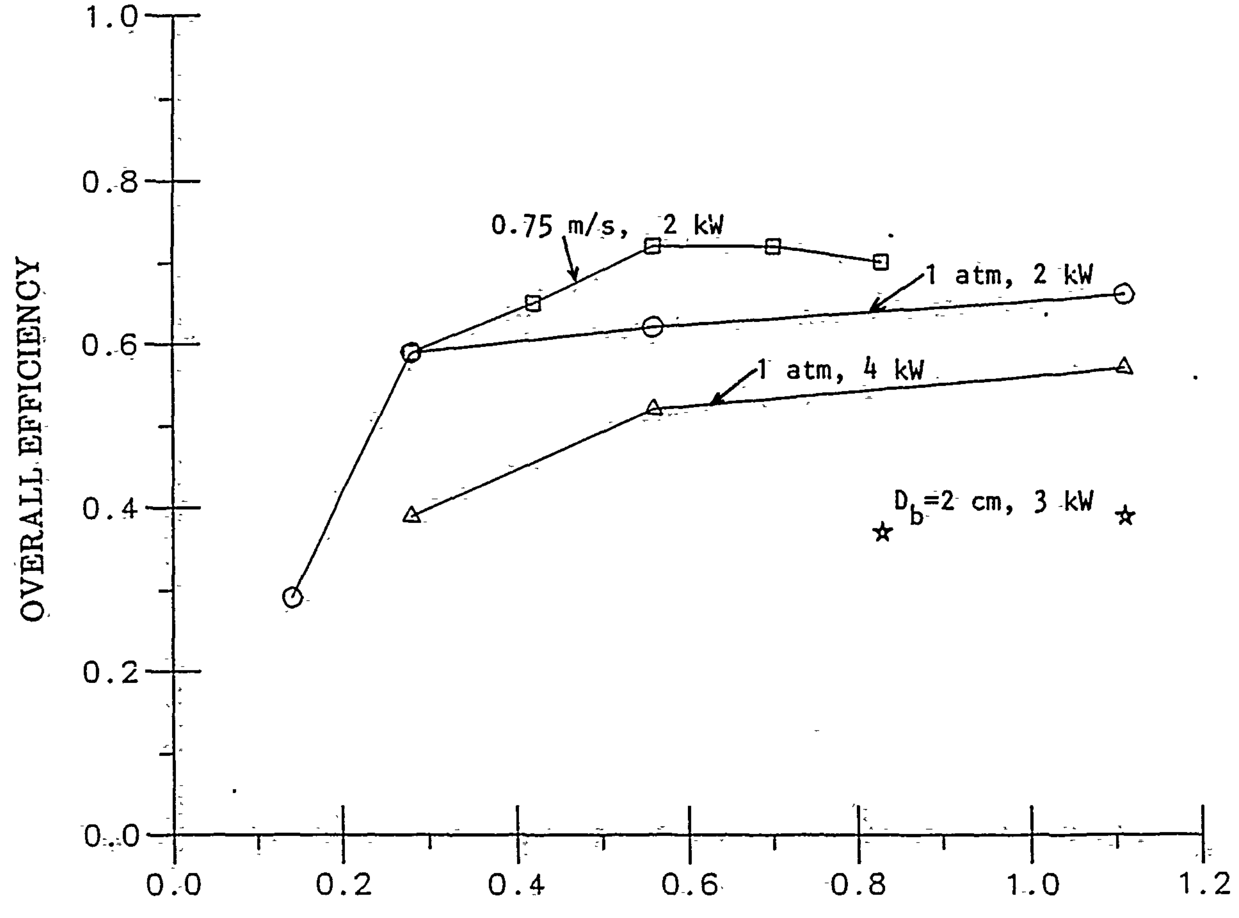

MASS FLOW RATE, g/s

Figure 32.Overall thermal efficiency as a function of mass flow rate.

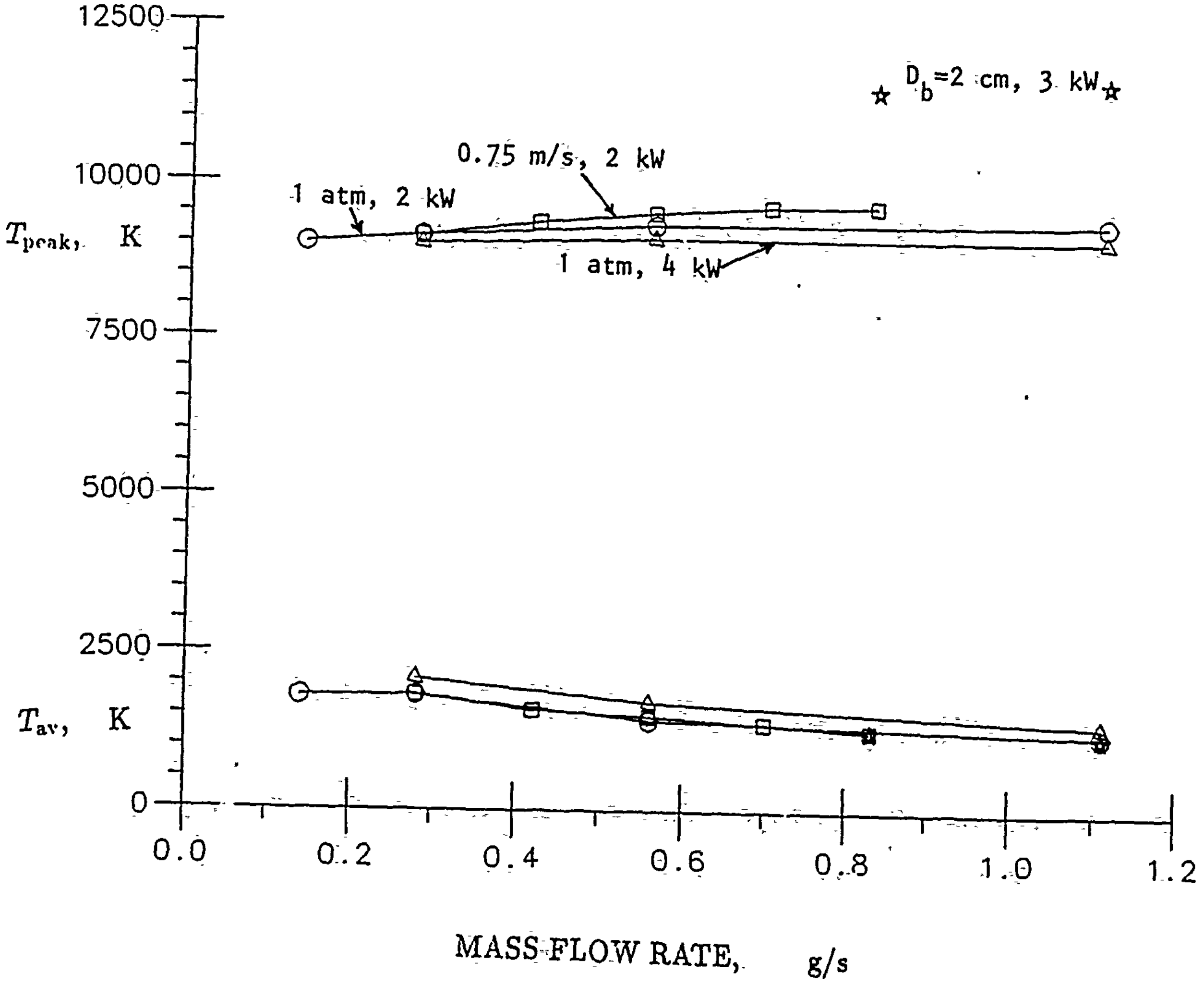

Figure 33. Peak and average gas temperatures as a function of mass flow rate.